



Title	Ternary platinum-cobalt-indium nanoalloy on ceria as a highly efficient catalyst for the oxidative dehydrogenation of propane using CO <sub>2</sub>
Author(s)	Xing, Feilong; Nakaya, Yuki; Yasumura, Shunsaku; Shimizu, Ken-ichi; Furukawa, Shinya
Citation	Nature Catalysis, 5(1), 55-65 <a href="https://doi.org/10.1038/s41929-021-00730-x">https://doi.org/10.1038/s41929-021-00730-x</a>
Issue Date	2022-01-27
Doc URL	<a href="http://hdl.handle.net/2115/86382">http://hdl.handle.net/2115/86382</a>
Rights	This version of the article has been accepted for publication, after peer review (when applicable) and is subject to Springer Nature 's AM terms of use, but is not the Version of Record and does not reflect post-acceptance improvements, or any corrections. The Version of Record is available online at: <a href="https://doi.org/10.1038/s41929-021-00730-x">https://doi.org/10.1038/s41929-021-00730-x</a>
Type	article (author version)
File Information	PtCoIn_MSf.pdf



[Instructions for use](#)

1  
2  
3  
4  
5  
6  
7  
8  
9  
10  
11  
12  
13  
14  
15  
16  
17  
18  
19  
20  
21  
22  
23  
24

# Platinum–cobalt–indium nanoalloy on ceria as a highly efficient catalyst for the oxidative dehydrogenation of propane using CO<sub>2</sub>

Feilong Xing,<sup>†</sup> Yuki Nakaya,<sup>†</sup> Shunsaku Yasumura,<sup>†</sup> Ken-ichi Shimizu,<sup>†,‡</sup>  
Shinya Furukawa<sup>\*,†,‡,§</sup>

<sup>†</sup> *Institute for Catalysis, Hokkaido University, N21, W10, Sapporo 001-0021, Japan*

<sup>‡</sup> *Elements Strategy Initiative for Catalysts and Batteries, Kyoto University, Katsura, Kyoto 615-8520, Japan*

<sup>§</sup> *Japan Science and Technology Agency, PRESTO, Chiyodaku, Tokyo 102-0076, Japan*

## **Corresponding authors**

Shinya Furukawa

Institute for Catalysis, Hokkaido University, N21, W10, Sapporo 001-0021, Japan

E-mail: furukawa@cat.hokudai.ac.jp,

Fax: +81-11-706-9163

25 **Abstract**

26 The oxidative dehydrogenation of propane using CO<sub>2</sub> (CO<sub>2</sub>-ODP) is a promising technique for  
27 high-yield propylene production and CO<sub>2</sub> utilization. Developing a highly efficient catalyst for  
28 CO<sub>2</sub>-ODP is of great interest and benefit to the chemical industry and for carbon recycling. However,  
29 the efficiency of the existing catalysts is limited. Here, we report a Pt–Co–In ternary nanoalloy on CeO<sub>2</sub>  
30 having a (Pt<sub>1-x</sub>Co<sub>x</sub>)<sub>2</sub>In<sub>3</sub> pseudo-binary alloy structure, which exhibits a considerably high catalytic  
31 activity, C<sub>3</sub>H<sub>6</sub> selectivity, stability, and CO<sub>2</sub> utilization efficiency at 550 °C. Alloying Pt with In and Co  
32 significantly improves the C<sub>3</sub>H<sub>6</sub> selectivity and CO<sub>2</sub> reduction ability, respectively. The Co species  
33 provide a high density of states near the Fermi level, which lowers the energy barrier of CO<sub>2</sub> reduction.  
34 The catalyst stability is drastically enhanced by combining the strong CO<sub>2</sub> activation ability of the alloy  
35 and the CeO<sub>2</sub> support capable of oxygen release, which facilitate Mars-van Krevelen-type coke  
36 combustion.

37

38 **Keywords:** propane dehydrogenation, CO<sub>2</sub>, ternary alloy, intermetallic, CeO<sub>2</sub>

39

40

41

42 Propylene is a very important raw materials for the production of a variety of petrochemicals in several  
43 industries.<sup>1</sup> The recent shift in the feedstock for steam crackers from oil-based naphtha to shale-based  
44 ethane has resulted in a significant gap between the limited supply of propylene and its increasing  
45 demand globally.<sup>2</sup> Therefore, the development of highly efficient technologies to meet the rising global  
46 demand for propylene is greatly desired.<sup>3</sup> Although the direct dehydrogenation of propane (DDP) has  
47 been studied and industrialized for this purpose, high reaction temperatures (typically  $\geq 650$  °C) are  
48 required to obtain a sufficiently high propylene yield due to the process's endothermicity.<sup>4</sup> Furthermore,  
49 the harsh conditions inevitably induce severe catalyst deactivation and the thermal decomposition of  
50 propylene, limiting the applicability of the approach. The oxidative dehydrogenation of propane using  
51 CO<sub>2</sub> as a mild oxidant (CO<sub>2</sub>-ODP:  $C_3H_8 + CO_2 \rightarrow C_3H_6 + CO + H_2O$ ) is a promising strategy for  
52 solving such issues.<sup>5, 6</sup> The equilibrium conversion of propane increases when dry reforming of C<sub>3</sub>H<sub>8</sub>  
53 proceeds in parallel ( $C_3H_8 + 3CO_2 \rightarrow 6CO + 4H_2$ ),<sup>7,8,9</sup> which can decrease the reaction temperature  
54 required to achieve a high propane conversion.<sup>7</sup> Moreover, CO<sub>2</sub> can remove the coke deposited on the  
55 catalyst surface via the Boudouard reaction ( $CO_2 + C \rightarrow 2CO$ ).<sup>10</sup> Unlike strong oxidants such as O<sub>2</sub>,  
56 CO<sub>2</sub> suppresses the over-oxidation of propylene and the catalyst itself, thus potentially providing an  
57 efficient catalytic system for propylene production. Moreover, the catalytic conversion of CO<sub>2</sub> into a  
58 value-added chemical is beneficial for carbon recycling and greenhouse gas reduction.<sup>11, 12</sup>

59 The previous studies on the CO<sub>2</sub>-ODP focused predominantly on early transition or typical metal  
60 oxides (Cr<sub>2</sub>O<sub>3</sub>, V<sub>2</sub>O<sub>5</sub>, Ga<sub>2</sub>O<sub>3</sub>, and In<sub>2</sub>O<sub>3</sub>)<sup>5, 13, 14, 15, 16</sup> and late transition metals (Pd, and Fe<sub>3</sub>Ni)<sup>7, 17</sup> as the  
61 main active species. Among these materials, chromium oxide species dispersed on mesoporous  
62 silica<sup>18,19</sup> showed the highest specific activity and good propylene selectivity (ca. 80%) at high propane  
63 conversion regions. However, these catalysts showed very low CO<sub>2</sub> conversion and rapid deactivation  
64 within a few hours. Although the transition metal catalysts exhibited much longer catalyst life, the  
65 conversions of propane and CO<sub>2</sub> were quite low (typically, <12%). In this context, to date, no catalyst  
66 has been reported that exhibits at the same time a high catalytic activity, selectivity, stability, and CO<sub>2</sub>  
67 utilization efficiency. The challenge is that the catalyst should simultaneously activate both propane and  
68 CO<sub>2</sub> without undesired side reactions and catalyst deactivation. Therefore, a multifunctional active  
69 material that successfully meets these requirements should be developed as an innovative catalyst for  
70 the CO<sub>2</sub>-ODP. Possible candidates are multimetallic alloys.<sup>20, 21, 22</sup> A highly efficient CO<sub>2</sub>-ODP may be  
71 realized based on an appropriate combination of elements that can facilitate C–H scission and CO<sub>2</sub>

72 capture/activation, as well as the inhibition of undesired over-dehydrogenation and C–C scission.

73 Motivated by this concept, we designed a ternary alloy catalyst consisting of three different classes  
74 of metals for the aforementioned functions in catalysis. First, Pt was chosen as the main active metal for  
75 the C–H scission because it is known to be highly active for C–H scission,<sup>23, 24</sup> while it is minimally  
76 active for the C–C scission compared to other transition metals.<sup>25</sup> Further, the late 3d transition metals  
77 such as Co, Ni, and Cu,<sup>26, 27</sup> which are efficient catalysts for CO<sub>2</sub> reduction, were chosen to accelerate  
78 CO<sub>2</sub> capture and activation. Finally, inert typical elements such as Ga, In, and Sn were considered to  
79 enhance the dehydrogenation selectivity, owing to an ensemble effect on alloying.<sup>28</sup> CeO<sub>2</sub> was also  
80 applied as the catalyst support to promote CO<sub>2</sub> capture and coke combustion, owing to its basicity and  
81 oxygen-releasing ability, respectively.<sup>7, 29</sup> In particular, we show that the combination of Pt, Co, In, and  
82 CeO<sub>2</sub> can afford the multiple functions required to achieve a highly efficient CO<sub>2</sub>-ODP, i.e., a  
83 remarkably active, selective, and stable catalysis is achieved using a Pt–Co–In/CeO<sub>2</sub> nanoalloy.

84

## 85 **Results**

### 86 **Characterization**

87 The Pt–Co–In/CeO<sub>2</sub> (Pt: 3wt%, Pt:Co:In = 1:1:2) catalyst was prepared by a conventional impregnation  
88 method using CeO<sub>2</sub> as the support. Figs 1a and b show the high-resolution high-angle annular dark field  
89 scanning transmission electron microscopy (HAADF-STEM) images of Pt–Co–In/CeO<sub>2</sub>. Small  
90 nanoparticles with diameters in the range of 2–3 nm were mainly observed on the CeO<sub>2</sub> support. The  
91 mean diameter (3.9 nm, Fig. 1c) was slightly higher than the size of major species because of the  
92 presence of a small amount of relatively large particles (10–16 nm). Since recent studies have  
93 demonstrated that reverse water-gas shift reaction<sup>30</sup> and propane dehydrogenation<sup>31, 32</sup> are structure  
94 sensitive (smaller particles afford higher activity), large particles (>10 nm) may have little contribution  
95 to the overall reaction rate in CO<sub>2</sub>-ODP. The elemental map acquired by energy-dispersive X-ray (EDX)  
96 analysis showed that the nanoparticles consisted of Pt, Co, and In, and some Co species were also  
97 present outside of the nanoparticles (Figs. 1d–h). The Pt:Co:In atomic ratios of the nanoparticles  
98 (regions 1–4, designated by dashed yellow squares in Figs. 1a and b) were approximately 1:0.5:2 (Fig.  
99 1i), where the Co content was lower than that supplied in the catalyst preparation (Pt:Co:In = 1:1:2).

100

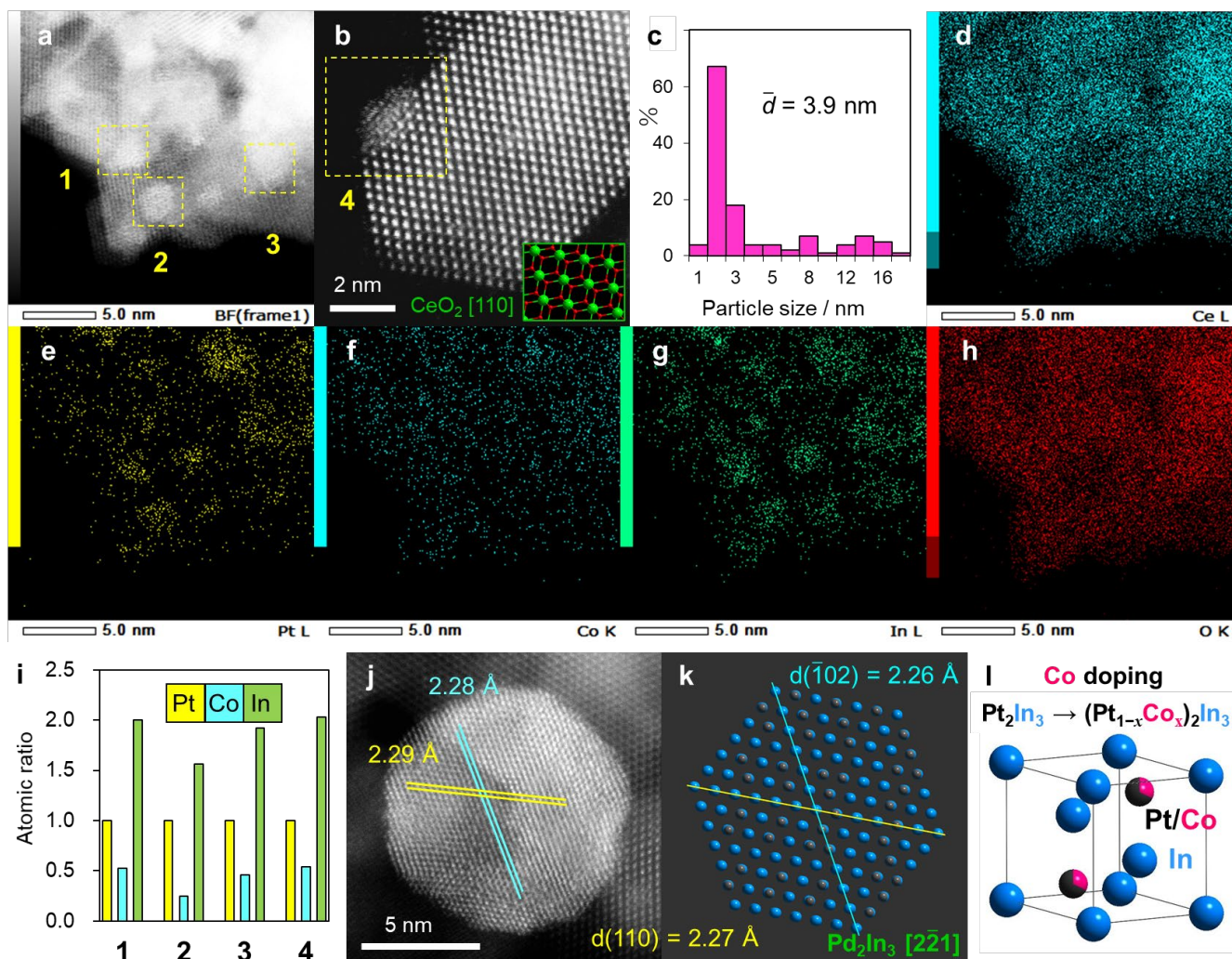


**Fig. 1: Characterization of Pt–Co–In/CeO<sub>2</sub>.** **a, b** HAADF-STEM image of Pt–Co–In/CeO<sub>2</sub> (Pt:Co:In =1:1:2). **c** Particle-size distribution. **d–h**, Elemental maps of **(d)** Ce, **(e)** Pt, **(f)** Co, **(g)** In, and **(h)** O in **a**, acquired by EDX. **i** Atomic ratios of Pt, Co, and, In present in the regions 1–4, designated by dotted yellow squares in **a** and **b**. **j** HAADF-STEM image of a single nanoparticle on Pt–Co–In/CeO<sub>2</sub>. **k** Crystal structure of the intermetallic Pt<sub>2</sub>In<sub>3</sub> viewed along the [2̄2̄1] direction. **l** Model of the (Pt<sub>1-x</sub>Co<sub>x</sub>)<sub>2</sub>In<sub>3</sub> pseudo-binary alloy structure with the crystal structure unit.

Therefore, some of the Co species appear to not be included in the nanoparticles and are highly dispersed on the CeO<sub>2</sub> support. Fig. 1j shows the STEM image of a single Pt–Co–In nanoparticle, where a crystal structure with interplanar distances of 2.28 and 2.29 Å was observed. These values were close to those of the (110) and (102) planes of intermetallic Pt<sub>2</sub>In<sub>3</sub> (Figs. 1j and k).<sup>33</sup> Considering that the atomic ratio of (Pt+Co):In is close to 2:3 (2:2.7), the nanoparticles likely have a (Pt<sub>1-x</sub>Co<sub>x</sub>)<sub>2</sub>In<sub>3</sub> pseudo-binary alloy structure, where some Pt atoms in Pt<sub>2</sub>In<sub>3</sub> are substituted by Co (Fig. 1l). Further, we performed an X-ray diffraction (XRD) analysis of Pt–Co–In/CeO<sub>2</sub>, from which a diffraction pattern

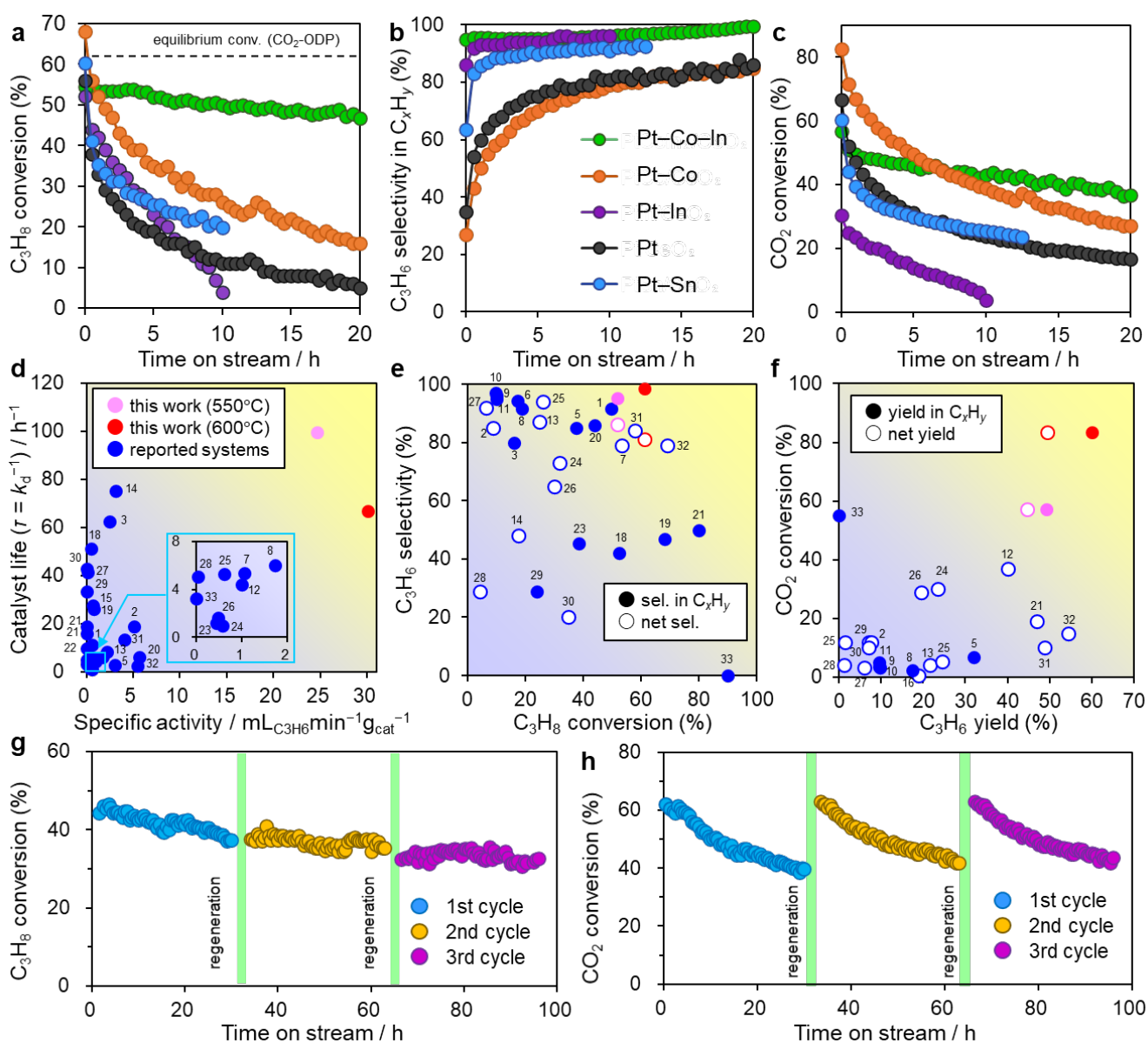
116 similar to that of Pt<sub>2</sub>In<sub>3</sub> was obtained, although the diffraction angles were slightly lower than those of  
117 pure Pt<sub>2</sub>In<sub>3</sub> (Supplementary Fig. 1). This indicates the lattice expansion of Pt<sub>2</sub>In<sub>3</sub> by Co doping and  
118 supports the formation of the (Pt<sub>1-x</sub>Co<sub>x</sub>)<sub>2</sub>In<sub>3</sub> pseudo-binary alloy structure. To obtain further structural  
119 information, X-ray absorption fine structure (XAFS) analysis was subsequently performed. The Pt–Co–  
120 In/CeO<sub>2</sub> sample was reduced in-situ by a flow of H<sub>2</sub> at 550°C for 0.5 h. The Pt L<sub>III</sub>-, Co K-, and In  
121 K-edge X-ray absorption near edge spectra (XANES) of the pretreated Pt–Co–In/CeO<sub>2</sub> were similar to  
122 those of the corresponding foils, indicating that these metals are reduced mostly to a zero-valent state  
123 (Supplementary Fig. 2). A small contribution of In<sub>2</sub>O<sub>3</sub> was observed in the In K-edge XANES  
124 (Supplementary Fig. 2) and extended XAFS (EXAFS) spectra (Supplementary Fig. 3, the Fourier  
125 transform of EXAFS is shown in Supplementary Fig. 4). This suggests that the residual In species,  
126 which did not participate in the alloy formation, is present as an oxide on CeO<sub>2</sub>. EXAFS curve-fitting  
127 (Supplementary Fig. 5 and Supplementary Table 1) suggested the presence of Pt–In (In–Pt) and Co–In  
128 (In–Co) scatterings. This result agrees with the formation of the (Pt<sub>1-x</sub>Co<sub>x</sub>)<sub>2</sub>In<sub>3</sub> pseudo-binary alloy  
129 structure and supports that Co was doped at the Pt sites of Pt<sub>2</sub>In<sub>3</sub>. For Co K-edge fitting, Co–Co  
130 scattering with an interatomic distance (*R*: 2.44) close to that of Co foil (2.49 Å) was also suggested.  
131 This indicates the presence of monometallic Co nanoparticles on CeO<sub>2</sub> and is consistent with the result  
132 of the HAADF-STEM-EDX analysis. In–O scattering was also derived for In K-edge fitting, indicating  
133 the presence of In<sub>2</sub>O<sub>3</sub> as observed for the XANES. Thus, the XAFS analysis demonstrated the formation  
134 of (Pt<sub>1-x</sub>Co<sub>x</sub>)<sub>2</sub>In<sub>3</sub> pseudo-binary alloy nanoparticles on CeO<sub>2</sub>. The residual Co and In species, which did  
135 not participate in alloy formation, remained as monometallic Co and In<sub>2</sub>O<sub>3</sub> nanoparticles. Besides, we  
136 conducted an X-ray photoelectron spectroscopy (XPS) analysis on the catalysts. Pt/CeO<sub>2</sub> and Pt–Co–  
137 In/CeO<sub>2</sub> showed similar Pt 4f<sub>7/2</sub> emissions at 71.6 and 71.4 eV, respectively, which are assigned to  
138 metallic Pt (Supplementary Fig. 6a).<sup>34</sup> The small negative shift indicates that Pt was slightly  
139 electron-enriched upon alloying with In and Co. The In 3d XPS spectrum showed that the surface In  
140 species was mainly metallic. A small part of In was oxidized (Supplementary Fig. 6b, In<sup>(0)</sup>: 443.5 eV  
141 and In<sup>3+</sup>: 444.5 eV),<sup>34</sup> which can be attributed to the ternary alloy phase and residual In<sub>2</sub>O<sub>3</sub>, respectively,  
142 as suggested by the XAFS study.

143

## 144 **Catalytic Reactions**

145 Afterward, the Pt–Co–In/CeO<sub>2</sub> catalyst was tested for the CO<sub>2</sub>-ODP at 550°C. Some Pt-based binary

146 alloy catalysts (Pt–M/CeO<sub>2</sub> : M = Co, In, and Sn), of which the Pt dispersion is similar to that of Pt–Co–  
 147 In/CeO<sub>2</sub> (Supplementary Table 2), and monometallic Pt/CeO<sub>2</sub> were examined to understand the  
 148 individual effect of each second metal. For all the catalysts, the products were CO, C<sub>3</sub>H<sub>6</sub>, C<sub>2</sub>H<sub>4</sub>, C<sub>2</sub>H<sub>6</sub>,  
 149 CH<sub>4</sub>, H<sub>2</sub>O, and H<sub>2</sub>. No other byproducts such as oxygenates were detected in the outlet gas  
 150 (Supplementary Fig. 7). Figs. 2a–c show the time course of C<sub>3</sub>H<sub>8</sub> conversion, C<sub>3</sub>H<sub>6</sub> selectivity in  
 151 hydrocarbons (C<sub>x</sub>H<sub>y</sub>), and CO<sub>2</sub> conversion, respectively (see Supplementary Fig. S8 for details of  
 152 equilibrium conversion). Although the Pt/CeO<sub>2</sub> and Pt–M/CeO<sub>2</sub> catalysts showed a high initial C<sub>3</sub>H<sub>8</sub>  
 153 conversion (52–68%), rapid deactivation occurred within 5–10 h. Pt–Sn, which is known to be selective  
 154 and stable for DDP,<sup>28</sup> was not effective for CO<sub>2</sub>-ODP.  
 155



156

157 **Fig. 2: Catalytic performance of Pt–Co–In/CeO<sub>2</sub> in the CO<sub>2</sub>-ODP.** Reaction conditions: catalyst  
158 amount, 100 mg; gas feed, C<sub>3</sub>H<sub>8</sub>:CO<sub>2</sub>:He = 5:5:10 mL·min<sup>-1</sup>; temperature, 550 °C. **a, b, c** Time course  
159 of **(a)** C<sub>3</sub>H<sub>8</sub> conversion, **(b)** C<sub>3</sub>H<sub>6</sub> selectivity, and **(c)** CO<sub>2</sub> conversion. **d, e, f** Comparison of the catalytic  
160 performances with those of reported systems: **(d)** specific activity vs. expected catalyst life, **(e)** C<sub>3</sub>H<sub>8</sub>  
161 conversion vs. C<sub>3</sub>H<sub>6</sub> selectivity, and **(f)** C<sub>3</sub>H<sub>6</sub> yield vs. CO<sub>2</sub> conversion. Numbers correspond to the  
162 entries in Supplementary Tables 4 and 5. Dashed curves indicate the iso-yield curves of C<sub>3</sub>H<sub>6</sub>. **g, h**  
163 Long-term stability test with catalyst regeneration: C<sub>3</sub>H<sub>8</sub>:CO<sub>2</sub>:He = 5:5:20 mL·min<sup>-1</sup>. Time course of **(g)**  
164 C<sub>3</sub>H<sub>8</sub> and **(h)** CO<sub>2</sub> conversions. Regeneration conditions: CO<sub>2</sub>:He = 5:20 mL·min<sup>-1</sup> for 5 h, followed by  
165 H<sub>2</sub>:He = 10:20 mL·min<sup>-1</sup> for 0.5 h at 550 °C.  
166

167 In contrast, Pt–Co–In/CeO<sub>2</sub> retained a high C<sub>3</sub>H<sub>8</sub> conversion (ca. 50%) for 20 h. Predictably, catalysts  
168 containing a typical metal (In or Sn) exhibited a high C<sub>3</sub>H<sub>6</sub> selectivity (82–95%), attributed to the  
169 ensemble effect by alloying, where the highest selectivity was obtained with Pt–Co–In (95%). Pt and  
170 Pt–Co showed very low C<sub>3</sub>H<sub>6</sub> selectivities (35 and 27%, respectively) at the beginning of the reaction,  
171 owing to undesired side reactions to generate C<sub>1</sub> and C<sub>2</sub> hydrocarbons (hydrogenolysis, Fig. S9). Pt and  
172 Pt–Co catalysts also showed a significant deviation of material balance from unity (e.g., for Pt, C<sub>x</sub>H<sub>y</sub>:  
173 0.71 and CO<sub>x</sub>: 1.31, Fig. S8), which suggests that dry reforming of C<sub>3</sub>H<sub>8</sub> to CO also occurred to a large  
174 extent. Conversely, the carbon balances in C<sub>x</sub>H<sub>y</sub> and CO<sub>x</sub> were close to unity for Pt–Co–In, indicating a  
175 minor contribution of dry reforming on the ternary alloy catalyst (Supplementary Fig. 10). The net C<sub>3</sub>H<sub>6</sub>  
176 selectivity and yield, which consider CO from C<sub>3</sub>H<sub>8</sub> as a byproduct, were still high (86–97%,  
177 Supplementary Fig. 11 and 47–44%, Supplementary Fig. 12, respectively). H<sub>2</sub> yield for Pt–Co–In was  
178 less than 5% (Supplementary Fig. 13), indicating that a large part of hydrogen derived from C<sub>3</sub>H<sub>8</sub> was  
179 consumed by reverse water-gas shift reaction. This also suggests that the contribution of DDP versus  
180 CO<sub>2</sub>-ODP to the overall C<sub>3</sub>H<sub>6</sub> production, which is reflected roughly by the H<sub>2</sub> yield/C<sub>3</sub>H<sub>6</sub> yield ratio,<sup>35</sup>  
181 was considerably low (~10%). Considering that H<sub>2</sub> can also be formed by dry reforming to a small  
182 extent, the actual contribution of DDP should be much lower than 10%. For the CO<sub>2</sub> conversion stability  
183 (Fig. 2c), a similar trend to that of C<sub>3</sub>H<sub>8</sub> was observed: only Pt–Co–In showed good stability, while  
184 other mono- and bimetallic catalysts were deactivated within 10 h. Interestingly, the initial conversion  
185 of CO<sub>2</sub> differed depending on the metal component in the following order: Pt–Co > Pt, Pt–Sn, Pt–Co–In  
186 >> Pt–In. This result implies that Co promotes CO<sub>2</sub> capture and activation as expected, and that alloying  
187 with In alone significantly reduces this ability. Therefore, alloying Pt with both Co and In may  
188 neutralize the negative effect of In, thereby promoting the CO<sub>2</sub> conversion, comparable to the level of

189 monometallic Pt. Thereafter, monometallic Co/CeO<sub>2</sub> and In/CeO<sub>2</sub> catalysts were also tested for the  
190 CO<sub>2</sub>-ODP as control experiments (Supplementary Fig. 14). Although Co/CeO<sub>2</sub> was active for both C<sub>3</sub>H<sub>8</sub>  
191 and CO<sub>2</sub> conversions at the beginning of the reaction, it rapidly deactivated within only 0.5 h (C<sub>3</sub>H<sub>8</sub>:  
192 48%→7%, CO<sub>2</sub>: 54%→22%). After the deactivation, Co/CeO<sub>2</sub> retained the low CO<sub>2</sub> conversion (22%),  
193 which is probably due to the contribution of Co oxide species to CO<sub>2</sub> reduction<sup>36,37</sup> (Co/SiO<sub>2</sub> was not  
194 fully reduced by reduction at 600°C; see H<sub>2</sub>-TPR, Supplementary Fig. 15). In/CeO<sub>2</sub> was almost inactive  
195 for both reactions. Therefore, the residual metallic Co and In oxide species in Pt–Co–In/CeO<sub>2</sub> are  
196 unlikely to contribute to the high catalytic performance. We performed further control experiments  
197 using physical mixtures of the binary and monometallic catalysts (Pt–Co/CeO<sub>2</sub>+In/CeO<sub>2</sub>, Pt–  
198 In/CeO<sub>2</sub>+Co/CeO<sub>2</sub>, and Co–In/CeO<sub>2</sub>+Pt/CeO<sub>2</sub>) and Pt–In+Co/CeO<sub>2</sub>, where the Co cation was loaded on  
199 Pt–In/CeO<sub>2</sub>. Their catalytic activities and stabilities were much lower than those of Pt–Co–In/CeO<sub>2</sub>  
200 (Supplementary Figs. 16–18), demonstrating that the ternary alloy structure with Co doped into Pt–In  
201 alloy is essential for a high catalytic performance. A temperature-programmed oxidation (TPO,  
202 Supplementary Fig. 19) and Raman analysis (Supplementary Fig. 20) of the spent catalysts after the 20  
203 h catalytic run showed almost no coke accumulation on Pt–Co–In/CeO<sub>2</sub>, unlike the case with other  
204 deactivated catalysts. The average coke selectivity was calculated at 10 h by dividing the mole of  
205 accumulated coke by the total mole of the converted C<sub>3</sub>H<sub>8</sub> and carbon number of C<sub>3</sub>H<sub>8</sub>, which was lower  
206 than 0.1% (Supplementary Table 3).

207 The obtained high catalytic performance of Pt–Co–In/CeO<sub>2</sub> was compared with a number of  
208 reported systems for the CO<sub>2</sub>-ODP, considering the activity, selectivity, stability, and CO<sub>2</sub> utilization  
209 efficiency (Supplementary Tables 4–5 and Supplementary Fig. 21 for details with references). For a  
210 better comparison, the catalytic performance of Pt–Co–In/CeO<sub>2</sub> at 600°C (Supplementary Fig. 22) was  
211 also included. For alkane dehydrogenation, high catalytic activity is often achieved at the expense of  
212 selectivity and stability via the triggering of undesired side reactions.<sup>38</sup> Therefore, plotting stability or  
213 selectivity versus activity can be a good indication of the overall performance. More specifically, the  
214 mean catalyst life as a reciprocal deactivation constant ( $\tau = k_d^{-1}$ ) versus specific activity  
215 ( $\text{mL}_{\text{C}_3\text{H}_8} \cdot \text{min}^{-1} \cdot \text{g}_{\text{cat}}^{-1}$ ) and the conversion–selectivity relationship were considered (Figs. 2d and e,  
216 respectively). The specific activity of our catalyst was approximately five times higher than the typical  
217 values ever reported. This outstanding high catalytic activity is attributed to the use of Pt as a main  
218 active metal for the selective CO<sub>2</sub>-ODP. Moreover, the mean catalyst life of our catalyst at 550°C was

219 also the highest among those ever reported. For the selectivity–conversion plot, we showed the two  
220 selectivity descriptions for better comparison with reported systems using each, i.e., that considering  
221 by-products other than  $C_xH_y$  such as CO (net  $C_3H_6$  selectivity) or not ( $C_3H_6$  selectivity in  $C_xH_y$ ). Our  
222 catalyst exhibited the highest  $C_3H_6$  selectivity (86% and 95% for open and filled circles, respectively) at  
223 a high  $C_3H_8$  conversion region ( $> 50\%$ ), indicating its significant ability to suppress undesired side  
224 reactions. Fig. 2f shows the plot of the  $CO_2$  conversion versus the  $C_3H_6$  yield, which reflects the  $CO_2$   
225 utilization efficiency. A high  $CO_2$  conversion with  $C_3H_6$  production in 1:1 stoichiometry (the  
226 upper-right direction in Fig. 2f) is preferred for a high  $CO_2$  utilization efficiency (see Equation 16 for  
227 the definition of  $CO_2$  utilization efficiency). In this context, our catalyst exhibited the highest  $CO_2$   
228 conversion and  $C_3H_6$  yield with near 1:1 stoichiometry among the typical systems ever reported, where  
229 the  $CO_2$  utilization efficiency was 53% at 550 °C and 70% at 600 °C (Supplementary Fig. 21c). We also  
230 examined the reusability and long-term stability of Pt–Co–In/CeO<sub>2</sub> by applying a regeneration process.  
231 The regeneration of deactivated catalysts typically uses oxygen or air to combust deposited carbon. In  
232 this study,  $CO_2$  was used instead as a soft oxidant for the Boudouard reaction and relatively easy  
233 handling. To switch the catalytic run to the regeneration process, only the supply of  $C_3H_8$  was cut off to  
234 feed  $CO_2/He$  for 5 h, followed by  $H_2$  reduction for 0.5 h at the same temperature. By this process, the  
235  $CO_2$  conversion was fully recovered, and it had no negative effect on the  $C_3H_8$  conversion (Figs. 2g and  
236 h, see Supplementary Fig. 23 for  $C_3H_6$  selectivity). Although a slight decrease in  $C_3H_8$  conversion was  
237 observed, the conversion reached a steady-state after 70 h and retained 33% conversion at 96 h. Thus,  
238 the Pt–Co–In/CeO<sub>2</sub> catalyst displayed multiple properties of outstanding catalytic activity, excellent  
239  $C_3H_6$  selectivity, high  $CO_2$  utilization efficiency, long-term stability, and reusability. In Fig. 2g,  $C_3H_8$   
240 conversion was not fully recovered under the regeneration condition, indicating that coke on the active  
241 site for  $C_3H_8$  dehydrogenation is relatively not easy to be removed compared with that of  $CO_2$  activation.  
242 We also performed a control experiment with a DDP– $CO_2$  cycle test on Pt–Co–In/CeO<sub>2</sub>, where the gas  
243 feed was switched from  $C_3H_8/He$  (2 h) to  $CO_2/He$  (0.5 h). Although the  $C_3H_8$  conversion decreased to  
244 near zero within 2 h in the absence of  $CO_2$ , it was recovered by the  $CO_2$  treatment (Supplementary Fig.  
245 24). Thus, the Pt–Co–In/CeO<sub>2</sub> catalyst is highly capable of coke combustion by  $CO_2$ , which enables  
246 continuous coke removal and long-term stability in  $CO_2$ -ODP.

247

248 **Mechanistic study**

249 Next, we performed a mechanistic study to profoundly understand the functions of Co, In, and CeO<sub>2</sub>  
250 in the catalysis. First, a kinetic analysis was conducted to understand the rate-determining step (RDS) of  
251 the CO<sub>2</sub>-ODP on Pt–Co–In/CeO<sub>2</sub>. The following reaction rate equation was considered for the  
252 CO<sub>2</sub>-ODP:  $r_x = kP_{\text{C}_3\text{H}_8}^\alpha P_{\text{CO}_2}^\beta$ , where  $r_x$  is the consumption rate of  $x$  ( $x = \text{C}_3\text{H}_8$  or  $\text{CO}_2$ ), and  $P_{\text{C}_3\text{H}_8}$   
253 and  $P_{\text{CO}_2}$  are the pressures of C<sub>3</sub>H<sub>8</sub> and CO<sub>2</sub>, respectively. The experimental reaction orders were  
254 positive and could be higher than unity for  $P_{\text{C}_3\text{H}_8}$ , while they were negative for  $P_{\text{CO}_2}$  (Table 1, see  
255 Supplementary Fig. 25 for details). Here, we considered a Langmuir–Hinshelwood mechanism  
256 involving the two-step dehydrogenation of C<sub>3</sub>H<sub>8</sub> to C<sub>3</sub>H<sub>6</sub>, CO<sub>2</sub> reduction to CO, and oxidation of the  
257 eliminated hydrogen to form water (Table 1). We solved the rate equation of each step by applying  
258 quasi-stationary approximation and site conservation condition (see Supplementary Note 1 for details).  
259 The ranges of predicted reaction orders were fully consistent with the experimental orders only when  
260 the CO<sub>2</sub> activation to form CO and O was regarded as the RDS (step 6 in Table 1). Besides, we  
261 conducted microkinetic modeling based on the transition state theory and steady-state approximation to  
262 estimate the forward and reverse reaction rates for each step (Supplementary Note 1 and Supplementary  
263 Table 6). For this modeling, some parameters calculated using density functional theory (DFT), such as  
264 activation energy (to be described later) and vibrational frequency, were used. As shown in Table 1  
265 (calculated reaction rate), step 6 showed the lowest rate. These results showed that the RDS of  
266 CO<sub>2</sub>-ODP on Pt–Co–In/CeO<sub>2</sub> was the CO<sub>2</sub> activation. Subsequently, the apparent activation energy  
267 ( $E_A^*$ ) was estimated for Pt–In/CeO<sub>2</sub> and Pt–Co–In/CeO<sub>2</sub> by Arrhenius-type plots. The  $E_A$  of CO<sub>2</sub>  
268 activation was significantly reduced by the incorporation of Co to Pt–In (168.8→138.3 kJ·mol<sup>-1</sup>, Table  
269 1 and Supplementary Fig. 26), which is consistent with the experimental trend of the CO<sub>2</sub> conversion  
270 and turnover frequency (TOF), as shown in Fig. 2c and Supplementary Fig. 27, respectively. We also  
271 simulated the dependences of the reaction rate on  $P_{\text{C}_3\text{H}_8}$  and temperature using the kinetic modeling,  
272 both of which agreed finely with the experimental trends (Supplementary Fig. 28; only slight deviations  
273 from the experimental values were observed, which may be due to errors in the DFT calculation). This  
274 result strongly supports the validity of our kinetic model. Thus, the kinetic analysis revealed that  
275 alloying with Co kinetically promoted the CO<sub>2</sub> activation, which is the RDS of the CO<sub>2</sub>-ODP.  
276 Compared with reported systems, Pt–Co–In/CeO<sub>2</sub> showed comparable  $E_A^*$ : for C<sub>3</sub>H<sub>8</sub> dehydrogenation  
277 (WO<sub>x</sub>–VO<sub>x</sub>/SiO<sub>2</sub>: 127–145 kJ·mol<sup>-1</sup>, Fe<sub>3</sub>Ni/CeO<sub>2</sub>: 115 kJ·mol<sup>-1</sup>), for CO<sub>2</sub> activation (Fe<sub>3</sub>Ni/CeO<sub>2</sub>: 135  
278 kJ·mol<sup>-1</sup>).

**Table 1: Summary of the kinetic study of CO<sub>2</sub>-ODP.**

$r_x = kP_{C_3H_8}^\alpha P_{CO_2}^\beta$			apparent activation energy ( $E_A^*$ )				
experimental reaction order <sup>a</sup>	$\alpha$	$\beta$	$E_A / \text{kJ} \cdot \text{mol}^{-1}$	experiment		DFT calculation	
				Pt–In	Pt–Co–In	Pt <sub>2</sub> In <sub>3</sub>	Pt <sub>2</sub> In <sub>3</sub> –Co
$x = C_3H_8$	0.56 ~ 1.05	-0.62 ~ 0.00	C <sub>3</sub> H <sub>8</sub>	144.4	122.8	140.1	117.5
$x = CO_2$	1.59	-0.94 ~ -0.14	CO <sub>2</sub>	168.8	138.3	169.1	135.1

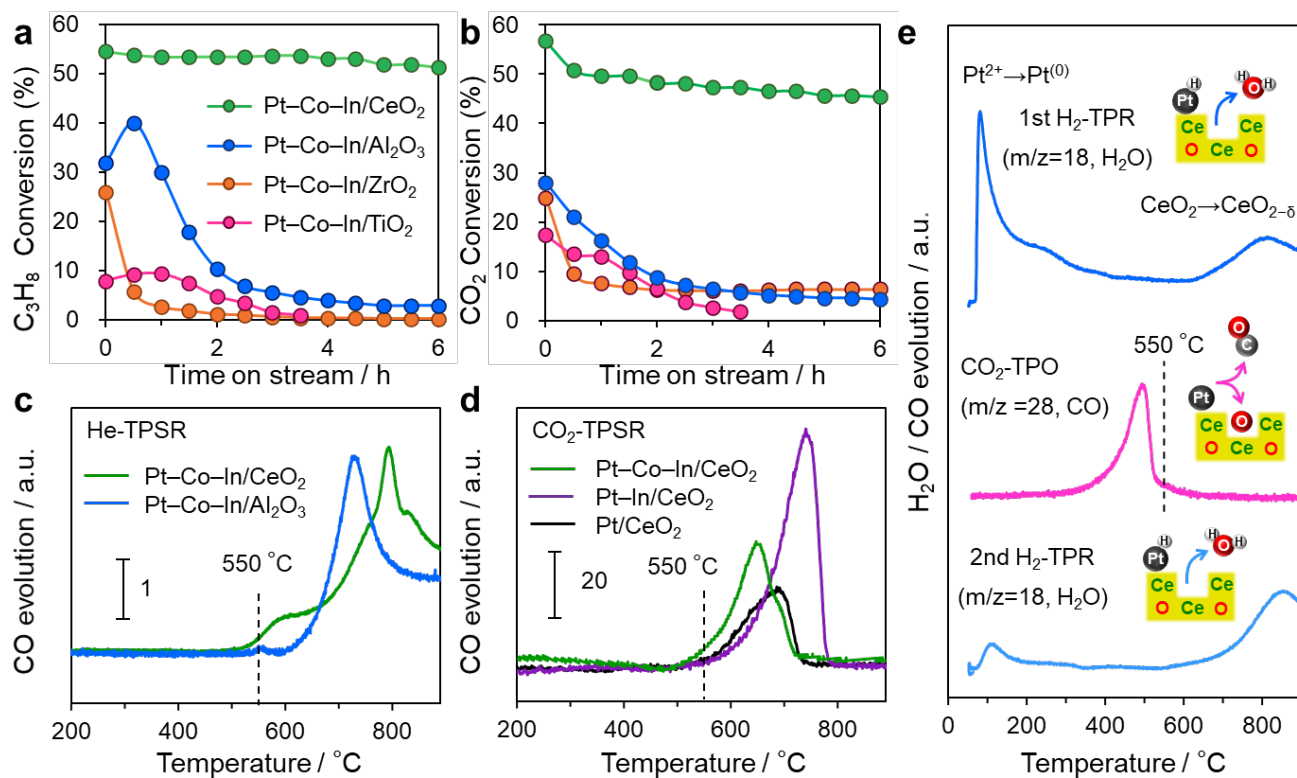
elementary steps in CO <sub>2</sub> -ODP	possible reaction order <sup>b</sup>		calculated reaction rate <sup>c</sup>			
	$\alpha$	$\beta$	$\vec{r}_f / \text{s}^{-1}$	$\vec{r}_r / \text{s}^{-1}$		
(1) C <sub>3</sub> H <sub>8</sub> + $\sigma \rightleftharpoons$ C <sub>3</sub> H <sub>8</sub> · $\sigma$		C <sub>3</sub> H <sub>8</sub> physisorption	1	-1 ~ 1	$3.87 \times 10^{12}$	$3.87 \times 10^{12}$
(2) C <sub>3</sub> H <sub>8</sub> · $\sigma$ + $\sigma \rightleftharpoons$ C <sub>3</sub> H <sub>7</sub> · $\sigma$ + H· $\sigma$		1st C–H activation	-1 ~ 1	-2 ~ 1	$1.86 \times 10^{-1}$	$1.86 \times 10^{-1}$
(3) C <sub>3</sub> H <sub>7</sub> · $\sigma$ + $\sigma \rightleftharpoons$ C <sub>3</sub> H <sub>6</sub> · $\sigma$ + H· $\sigma$		2nd C–H activation	-1 ~ 1	-1.5~1.5	$1.26 \times 10^{-3}$	$1.25 \times 10^{-3}$
(4) CO <sub>2</sub> + $\sigma \rightleftharpoons$ CO <sub>2</sub> · $\sigma$		CO <sub>2</sub> physisorption	-1 ~ 1	1	$3.87 \times 10^{12}$	$3.87 \times 10^{12}$
(5) CO <sub>2</sub> · $\sigma \rightleftharpoons$ CO <sub>2</sub> <sup>*</sup> · $\sigma$		CO <sub>2</sub> chemisorption	-1 ~ 1	0 ~ 1	$2.67 \times 10^2$	$2.67 \times 10^2$
(6) CO <sub>2</sub> <sup>*</sup> · $\sigma \rightleftharpoons$ CO· $\sigma$ + O· $\sigma$		CO <sub>2</sub> activation	<b>-2 ~ -2</b>	<b>-1 ~ -1</b>	<b><math>1.87 \times 10^{-5}</math></b>	<b><math>2.67 \times 10^{-6}</math></b>
(7) H· $\sigma$ + O· $\sigma \rightleftharpoons$ OH· $\sigma$ + $\sigma$		OH formation	-1.5~1.5	-1 ~ 1	$3.46 \times 10^{-4}$	$3.30 \times 10^{-4}$
(8) OH· $\sigma$ + O· $\sigma \rightleftharpoons$ H <sub>2</sub> O· $\sigma$ + $\sigma$		H <sub>2</sub> O formation	-1 ~ 1	-1 ~ 1	$1.02 \times 10^{-1}$	$1.02 \times 10^{-1}$
(9) C <sub>3</sub> H <sub>6</sub> · $\sigma \rightleftharpoons$ C <sub>3</sub> H <sub>6</sub> + $\sigma$		C <sub>3</sub> H <sub>6</sub> desorption	0 ~ 1	0 ~ 1.5	$1.61 \times 10^{11}$	$1.61 \times 10^{11}$
(10) CO· $\sigma \rightleftharpoons$ CO + $\sigma$		CO desorption	0 ~ 2	0 ~ 1	$1.61 \times 10^{11}$	$1.61 \times 10^{11}$
(11) H <sub>2</sub> O· $\sigma \rightleftharpoons$ H <sub>2</sub> O + $\sigma$		H <sub>2</sub> O desorption	0 ~ 1	0 ~ 1	$1.61 \times 10^{11}$	$1.61 \times 10^{11}$

<sup>a</sup>  $r_x$  was determined experimentally by the consumption rate of  $x$ . <sup>b</sup> Estimated by quasi-stationary approximation. Order ranges consistent with the experiment are shown in bold. <sup>c</sup> Calculated by microkinetic modeling using DFT-derived parameters:  $\vec{r}_f$  and  $\vec{r}_r$  indicate the reaction rates per one active site (TOF) for the forward and reverse directions, respectively. The lowest value corresponding to the RDS is shown in bold.

280

281 We subsequently examined a series of Pt–Co–In catalysts using various supports, such as Al<sub>2</sub>O<sub>3</sub>,  
 282 TiO<sub>2</sub>, and ZrO<sub>2</sub>, so that the role of the CeO<sub>2</sub> support was clarified. Although these catalysts showed  
 283 moderate initial conversions of C<sub>3</sub>H<sub>8</sub> and CO<sub>2</sub>, rapid deactivation occurred within 1–2 h (Figs. 3a and b).  
 284 This result strongly indicates that the role of CeO<sub>2</sub> is to significantly enhance the catalyst stability; this  
 285 is probably attributed to its coke combustion ability, as mentioned above. To confirm this ability,  
 286 temperature-programmed surface reactions (TPSRs) were conducted using the coked catalysts under He  
 287 and CO<sub>2</sub> flows. The coked Pt–Co–In/CeO<sub>2</sub> evolved CO from 500 °C even in the absence of CO<sub>2</sub>  
 288 (He-TPSR, Fig. 3c), whereas the coked Pt–Co–In/Al<sub>2</sub>O<sub>3</sub> showed almost no CO evolution up to 600°C.

289



290

291 **Fig. 3: Effect of the catalyst support and TPSR on the coked catalysts. a, b** (a)  $C_3H_8$  and (b)  $CO_2$   
 292 conversions in  $CO_2$ -ODP on the Pt–Co–In catalysts using various supports. **c** He-TPSR on the coked  
 293 Pt–Co–In/CeO<sub>2</sub> (used in DDP for 2 h) and Pt–Co–In /Al<sub>2</sub>O<sub>3</sub> (used in  $CO_2$ -ODP for 2 h) catalysts. **d**  
 294  $CO_2$ -TPSR on the coked Pt/CeO<sub>2</sub>, Pt–In/CeO<sub>2</sub> (used in  $CO_2$ -ODP for 2 h), and Pt–Co–In/CeO<sub>2</sub> (used in  
 295 DDP for 2 h) catalysts. CO evolution was quantified by the mass intensity of  $m/z = 28$ . **e**  $CO_2$ -titration  
 296 (TPO) experiment for the oxygen vacancy of CeO<sub>2</sub> using Pt/CeO<sub>2</sub>.

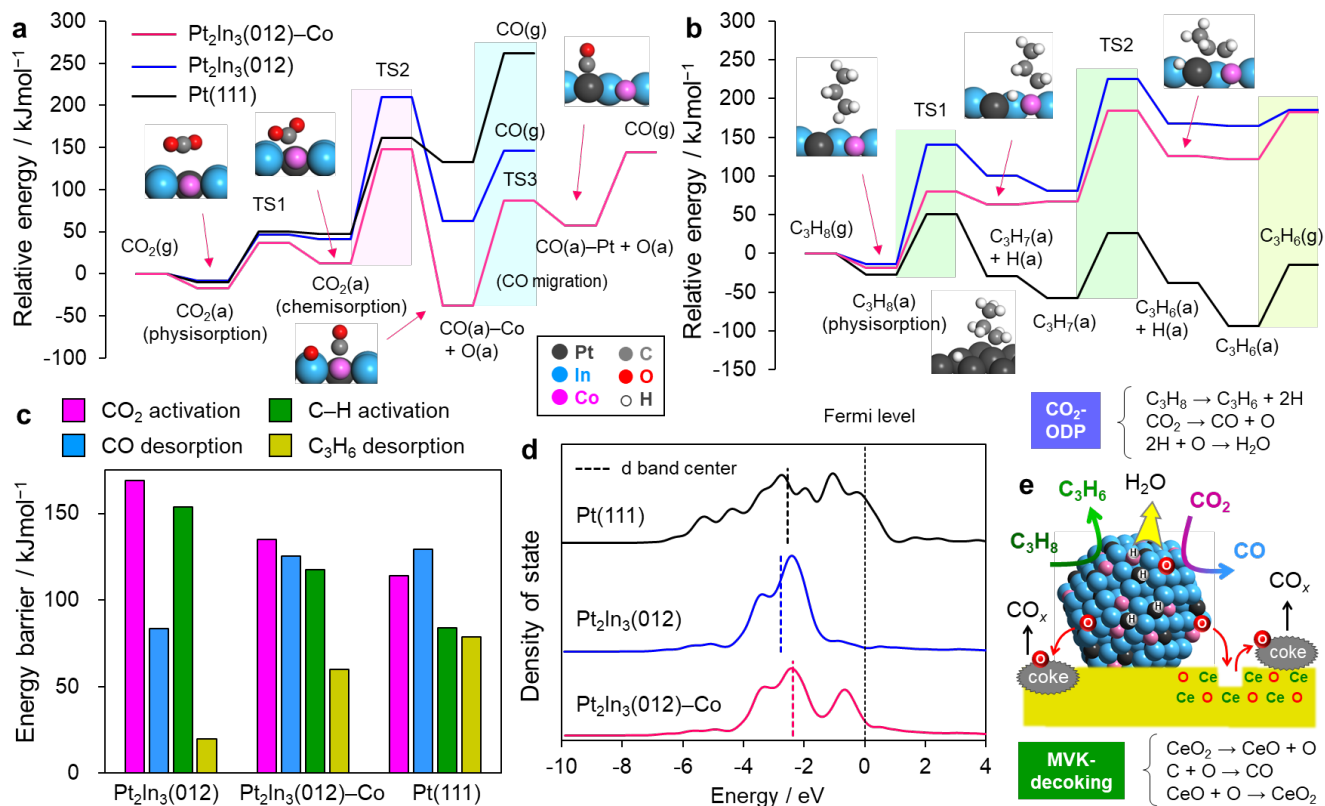
297

298 The CO evolution from the coked Pt–Co–In/CeO<sub>2</sub> between 500 and 600 °C can be attributed to the coke  
 299 combustion by the lattice oxygen of CeO<sub>2</sub>. Thus, CeO<sub>2</sub> can remove coke at the reaction temperature of  
 300  $CO_2$ -ODP (550 °C), while Al<sub>2</sub>O<sub>3</sub> cannot, which agrees with the stability trend in  $CO_2$ -ODP.  
 301 Interestingly, intense CO evolution was observed from 600 °C for both catalysts, which might be due to  
 302 the coke combustion by the oxygen atoms of the surface hydroxyl groups. When the TPSR experiment  
 303 for the coked Pt–Co–In/CeO<sub>2</sub> was performed in the presence of  $CO_2$  ( $CO_2$ -TPSR, Fig. 3d), a  
 304 considerably large amount of CO (see the scale bars) was evolved from 500 °C, and the coke was  
 305 completely combusted at 700 °C. This is clearly due to the continuous oxygen supply from  $CO_2$ . The  
 306 corresponding TPSR for the coked Pt/CeO<sub>2</sub> and Pt–In/CeO<sub>2</sub> showed similar CO evolutions at high  
 307 temperatures (peak temperature: Pt–Co–In < Pt < Pt–In), although a low evolution was observed at  
 308 550 °C. These results are roughly consistent with the deactivation trend (Pt–Co–In < Pt, Pt–In, Fig. 2a)

309 and the CO<sub>2</sub> reducing ability (Pt–Co–In, Pt > Pt–In, Fig. 2c), which reflects the coke combustion  
310 abilities of these catalysts. Based on these results, we concluded that the coke combustion ability  
311 depended on the CO<sub>2</sub> reducing ability of the metal nanoparticles, as well as the oxygen-releasing ability  
312 of CeO<sub>2</sub>. The concert of the ternary alloy and the specific character of the CeO<sub>2</sub> support enabled the  
313 continuous self-regeneration function and the remarkably high coke resistance. Furthermore, we verified  
314 the filling of oxygen vacancy after the lattice oxygen consumption of CeO<sub>2</sub> using a CO<sub>2</sub>-titration (TPO)  
315 technique and Pt/CeO<sub>2</sub>. As shown in Fig. 3e, oxygen vacancies of CeO<sub>2</sub> were obtained by H<sub>2</sub>-TPR,  
316 followed by cooling and subsequent CO<sub>2</sub>-TPO. CO evolution was completed by 550 °C, indicating that  
317 CO<sub>2</sub> was divided into CO and O. The oxygen atoms were left on the catalyst. H<sub>2</sub>-TPR was repeated after  
318 CO<sub>2</sub>-TPO and cooling, where the reduction peak of CeO<sub>2</sub> appeared again (Fig. 3e). These results  
319 strongly support that the oxygen atoms derived from CO<sub>2</sub> refill the oxygen vacancies of CeO<sub>2</sub>.

320 Finally, we conducted DFT calculations to understand the role of the Pt–Co–In ternary alloy in the  
321 enhanced catalysis. As a model of the Pt–Co–In alloy surface, the stable (012) surface of intermetallic  
322 Pt<sub>2</sub>In<sub>3</sub> was considered and one of the surface Pt atoms was replaced with Co, hereafter denoted as  
323 Pt<sub>2</sub>In<sub>3</sub>(012)–Co. Unmodified Pt<sub>2</sub>In<sub>3</sub>(012) and monometallic Pt(111) surfaces were also considered for  
324 comparison. CO<sub>2</sub> reduction to CO, C<sub>3</sub>H<sub>8</sub> dehydrogenation to C<sub>3</sub>H<sub>6</sub>, H<sub>2</sub>O formation, and H<sub>2</sub>  
325 recombination were considered on these surfaces (see Supplementary Figs. 29–37 for detailed structures  
326 and Supplementary Fig. 38 for Gibbs free energy changes). Fig. 4a shows the energy diagram of CO<sub>2</sub>  
327 reduction, where CO<sub>2</sub> was first physisorbed, then chemisorbed with a bent sp<sup>2</sup>-like conformation,  
328 followed by C–O bond scission to form CO and O, and lastly, CO desorption. The chemisorption was  
329 endothermic and required moderate energy barriers of 55–57 kJ·mol<sup>-1</sup>. For Pt<sub>2</sub>In<sub>3</sub> and Pt<sub>2</sub>In<sub>3</sub>–Co, the  
330 subsequent C–O scission generated CO on a top site of Pt/Co and O at an In–In bridge site, which was  
331 more stable than those on Pt(111), probably due to the oxophilicity of In. CO was considerably more  
332 stable on Co than on Pt; therefore, the direct desorption of CO from the Co site required a high amount  
333 of energy (182.3 kJ·mol<sup>-1</sup>). Relatively-low energy desorption is still allowed when CO migrates to the  
334 neighboring Pt site. However, the microkinetic modeling showed that the constant and reaction rate for  
335 the desorption of product molecules were considerably high (Table 1 and Supplementary Table 6) due  
336 to the huge contribution of the translational partition function of gas-phase molecules at high  
337 temperatures.

338



339

340 **Fig. 4: DFT calculations and reaction mechanism: a, b** Energy diagrams of (a) CO<sub>2</sub> reduction to CO  
 341 and O and (b) C<sub>3</sub>H<sub>8</sub> dehydrogenation to C<sub>3</sub>H<sub>6</sub> on Pt(111), Pt<sub>2</sub>In<sub>3</sub>(012), and Pt<sub>2</sub>In<sub>3</sub>(012)-Co. **c** Summary  
 342 of the energy barriers on each surface. For Pt<sub>2</sub>In<sub>3</sub>(012)-Co, the energy barrier of CO migration was  
 343 regarded as a desorption barrier. **d** Density of states projected on the d orbitals of the surface atoms of  
 344 Pt(111), Pt<sub>2</sub>In<sub>3</sub>(012), and Pt<sub>2</sub>In<sub>3</sub>(012)-Co slabs. **e** Schematic illustration of the reaction mechanism of  
 345 CO<sub>2</sub>-ODP on Pt-Co-In/CeO<sub>2</sub> with Mars-van Krevelen-type decoking by CeO<sub>2</sub>.

346

347 Thus, the direct desorption of CO from the Co site can smoothly occur even with the large energy  
 348 barrier. Fig. 4b represents the energy diagram of C<sub>3</sub>H<sub>8</sub> dehydrogenation, where two H atoms of C<sub>3</sub>H<sub>8</sub>  
 349 are subsequently eliminated and moved to infinity (opposite surface of the slab). The two C-H activations  
 350 were endothermic on the Pt<sub>2</sub>In<sub>3</sub>-based surfaces, whereas they were slightly exothermic on Pt(111),  
 351 which may be dependent on whether the eliminated H atoms were located on a less stable Pt-Pt(Co)  
 352 bridge site or on a highly stable Pt<sub>3</sub> hollow site. The high energy of the unstable H can be released after  
 353 each C-H scission using the subsequent oxidation reaction (H+O→OH, ΔE = -86 or -115 kJmol<sup>-1</sup>,  
 354 Supplementary Fig. 38a and Supplementary Tables 7-9). Thus, the net energy barriers for the “oxidative  
 355 dehydrogenation of C<sub>3</sub>H<sub>8</sub> (C<sub>3</sub>H<sub>8</sub> + O → C<sub>3</sub>H<sub>6</sub> + H<sub>2</sub>O)” on Pt<sub>2</sub>In<sub>3</sub>-based surface is not higher than that of  
 356 C-O scission (Supplementary Fig. 39). Fig. 4c. summarizes the major energy barriers on each surface.  
 357 The Pt(111) surface was more active than the Pt<sub>2</sub>In<sub>3</sub>-based surfaces for C-H and CO<sub>2</sub> activations, while

358 CO desorption showed the highest energy barrier. For Pt<sub>2</sub>In<sub>3</sub>(012), CO<sub>2</sub> activation required a high  
359 energy barrier of 169.1 kJ·mol<sup>-1</sup>, which agreed finely with the experimental  $E_A^*$  (168.8 kJ·mol<sup>-1</sup>, Table  
360 1 and Supplementary Fig. 26) and with the low CO<sub>2</sub> conversion and TOF of Pt–In/CeO<sub>2</sub>. (Figs. 2c and  
361 Supplementary Fig. 27). The  $E_A$  of CO<sub>2</sub> activation was significantly decreased to 135.1 kJ·mol<sup>-1</sup> on  
362 Pt<sub>2</sub>In<sub>3</sub>(012)–Co, which is also consistent with the experimental  $E_A^*$  (138.3 kJ·mol<sup>-1</sup>, Table 1) and the  
363 significantly improved CO<sub>2</sub> conversion/TOF (Figs. 2c and Supplementary Fig. 27) by Co-substitution.  
364 Good agreements were also obtained between the theoretical and experimental  $E_A^*$  values for C–H  
365 activation (Table 1), demonstrating the validity of our calculation. The CO<sub>2</sub> activation still provided the  
366 highest energy barrier on Pt<sub>2</sub>In<sub>3</sub>(012)–Co, which is consistent with the fact that this process is the RDS.  
367 The significant decrease in the energy barriers of C–H and CO<sub>2</sub> activations by Co-substitution can be  
368 explained by the lowering of the final state energies (Fig. 4b) in line with the Brønsted–Evans–Polanyi  
369 relationship.<sup>39</sup> The Co atom strongly captures the C and/or H atom of the adsorbate, thus stabilizing the  
370 adsorbate state. The stronger adsorption on Co can be rationalized by the d band structure of alloys, as  
371 shown in Fig. 4d. Alloying Pt with In decreased the d band width and the density of states near the  
372 Fermi level. This change weakens the metal–adsorbate bonding in accordance with the d band  
373 theory.<sup>40,41</sup> In contrast, Pt<sub>2</sub>In<sub>3</sub>(012)–Co has a high density of states derived from the Co 3d orbitals near  
374 the Fermi level, which recovers the adsorption strengths of C and H, hence promoting the conversion of  
375 CO<sub>2</sub> and C<sub>3</sub>H<sub>8</sub>. Thus, the DFT calculations well supported the experimental results and clarified the role  
376 of Co in the enhanced catalysis.

377 Overall, the reaction mechanism of CO<sub>2</sub>-ODP on Pt–Co–In/CeO<sub>2</sub> and the roles of the ternary alloy  
378 phase and the CeO<sub>2</sub> support are summarized in Fig. 4e. Both the C<sub>3</sub>H<sub>8</sub> dehydrogenation and CO<sub>2</sub>  
379 reduction smoothly proceed on the Pt–Co active site to form 2H and O, as well as the main products:  
380 C<sub>3</sub>H<sub>6</sub> and CO. Alloying with In enhances the C<sub>3</sub>H<sub>6</sub> selectivity due to the ensemble effect and decreases  
381 the amount of coke that accumulates on the catalyst surface. The doped Co improves the adsorption  
382 strengths of the C and H species, which promotes the activation of C<sub>3</sub>H<sub>8</sub> and CO<sub>2</sub>. The O atoms oxidize  
383 the eliminated H to form H<sub>2</sub>O or combust coke on the alloy surface or neighboring CeO<sub>2</sub> sites. Note that  
384 coke combustion is allowed when CO<sub>2</sub> conversion is higher than C<sub>3</sub>H<sub>8</sub> conversion because of the  
385 stoichiometry of the CO<sub>2</sub>-ODP. Coke can be combusted also by the lattice oxygen of CeO<sub>2</sub>, where CeO<sub>2</sub>  
386 is partially reduced to form an oxygen vacancy. This oxygen vacancy is refilled by an O atom derived  
387 from CO<sub>2</sub> activation, enabling continuous coke combustion through the redox of CeO<sub>2</sub>. Thus, CeO<sub>2</sub> can

388 facilitate coke combustion via a Mars-van Krevelen-type mechanism,<sup>17</sup> which significantly enhances the  
389 coke resistance and catalyst stability. Further information on the reaction mechanism can be obtained  
390 from the results of DDP over Pt–Co–In/CeO<sub>2</sub> shown in Supplementary Fig. 24. It is worth noting that no  
391 CO<sub>x</sub> (CO and CO<sub>2</sub>) was formed at all during DDP, indicating that lattice oxygen of CeO<sub>2</sub> does not  
392 combust C<sub>x</sub>H<sub>y</sub>. Thus, only carbonaceous species can be combusted by surface oxygen atom or lattice  
393 oxygen of CeO<sub>2</sub>. Besides, C<sub>3</sub>H<sub>8</sub> conversion in DDP at 550°C was relatively high (30%) and close the  
394 equilibrium conversion (43%, Supplementary Fig. 1) at the beginning of the reaction. This indicates that  
395 Pt–Co–In/CeO<sub>2</sub> possesses a high catalytic activity for C–H activation even in the absence of CO<sub>2</sub>,  
396 although it was immediately deactivated due to the lack of coke combustion. These results suggest that  
397 CO<sub>2</sub> does not drastically change the kinetics of the dehydrogenation step, while mainly shifts the  
398 equilibrium limitation. Thus, C<sub>3</sub>H<sub>8</sub> dehydrogenation and CO<sub>2</sub> conversion are parallel to each other and  
399 linked by the hydrogen oxidation processes, which is consistent finely with the mechanism proposed in  
400 this study.

401

## 402 **Discussion**

403 In summary, we designed and prepared a Pt–Co–In ternary alloy on CeO<sub>2</sub> as a highly efficient catalyst  
404 for the CO<sub>2</sub>-ODP. This material comprises small nanoparticles (2–3 nm) with a (Pt<sub>1-x</sub>Co<sub>x</sub>)<sub>2</sub>In<sub>3</sub>  
405 pseudo-binary alloy structure, where Pt, Co, and In are adjacent to each other on an atomic level. Pt–  
406 Co–In/CeO<sub>2</sub> exhibits outstanding catalytic activity, C<sub>3</sub>H<sub>6</sub> selectivity, long-term stability, and CO<sub>2</sub>  
407 utilization efficiency, all of which are greater than typical values ever reported. Alloying Pt with In and  
408 Co significantly enhances the selectivity and activity, respectively, while the CeO<sub>2</sub> support drastically  
409 improves the catalyst stability by Mars-van Krevelen-type coke combustion. The results obtained in this  
410 study provide not only a highly efficient catalytic system for alkane dehydrogenation and CO<sub>2</sub> reduction,  
411 but also significant insights for material design based on multimetallic alloys.

412

## 413 **Methods**

### 414 **Catalysts preparation**

415 Pt/CeO<sub>2</sub>, Pt–Co/CeO<sub>2</sub>, Pt–In/CeO<sub>2</sub>, Pt–Sn/CeO<sub>2</sub>, and Pt–Co–In/CeO<sub>2</sub> (Pt: 3 wt%) were prepared by a  
416 conventional impregnation method using H<sub>2</sub>PtCl<sub>6</sub> (aqueous solution, Kojima Chemicals, Pt 8.77 wt%),  
417 In(NO<sub>3</sub>)<sub>3</sub>·3H<sub>2</sub>O, Co(NO<sub>3</sub>)<sub>2</sub>·6H<sub>2</sub>O, and SnCl<sub>2</sub> as metal precursors. The CeO<sub>2</sub> support (JRC-CEO-2, S<sub>BET</sub>=

418 123.1 m<sup>2</sup>g<sup>-1</sup>) was added to a vigorously stirred aqueous solution (50 mL H<sub>2</sub>O per gram of CeO<sub>2</sub>)  
419 containing Pt and the corresponding second and/or third metal precursor(s) (Pt:Co =1:1, Pt:In =1:1,  
420 Pt:Sn = 1:1, and Pt:Co:In =1:1:2), followed by stirring for 3 h at room temperature. The mixture was  
421 dried under a reduced pressure at 50 °C using a rotary evaporator, followed by calcination under  
422 flowing air at 500°C for 1 h and reduction under flowing H<sub>2</sub> (50 mL/min) at 600 °C for 1 h. Co/CeO<sub>2</sub>  
423 and In/CeO<sub>2</sub> were prepared by a similar method, where the amounts of Co and In were adjusted to be  
424 equal to those included in Pt–Co–In/CeO<sub>2</sub>. A series of Pt–Co–In catalysts supported on various oxides  
425 other than CeO<sub>2</sub> (Pt–Co–In/MO<sub>x</sub>, where MO<sub>x</sub> = Al<sub>2</sub>O<sub>3</sub> (prepared by calcination of boehmite [ $\gamma$ -AlOOH,  
426 supplied by SASOL chemicals] at 900 °C for 3 h,  $\gamma$ -phase), TiO<sub>2</sub> (P25,  $S_{\text{BET}}$ = 35-65 m<sup>2</sup>g<sup>-1</sup>,  
427 anatase+rutile), ZrO<sub>2</sub> (JRC-ZRO-6,  $S_{\text{BET}}$ = 279.3 m<sup>2</sup>g<sup>-1</sup>); Pt:Co:In = 1:1:2, Pt: 3 wt%) was also prepared  
428 by the same method mentioned above. Pt–In+Co /CeO<sub>2</sub> was prepared as a control catalyst having a Pt–  
429 In alloy phase and cationic Co, by impregnating the reduced Pt–In/CeO<sub>2</sub> with an aqueous solution of  
430 Co(NO<sub>3</sub>)<sub>2</sub>·6H<sub>2</sub>O so that the final Pt:Co:In ratio became 1:1:2. Comparing the catalytic performances of  
431 Pt–Co–In/CeO<sub>2</sub> and Pt–In/CeO<sub>2</sub>+Co allows to understand whether Co should be included in the alloy  
432 phase or not for enhanced catalysis.

433

### 434 **Characterization**

435 The crystal structure of the prepared catalyst was examined by powder X-ray diffraction (XRD) using a  
436 Rigaku MiniFlex II/AP diffractometer with Cu K $\alpha$  radiation. High-angle annular dark field scanning  
437 transmission electron microscopy (HAADFSTEM) was carried out using a JEOL JEM-ARM200 M  
438 microscope equipped with an energy dispersive X-ray (EDX) analyzer (EX24221M1G5T). STEM  
439 analysis was performed at an accelerating voltage of 200 kV. To prepare the TEM specimen, all samples  
440 were sonicated in ethanol and then dispersed on a Mo grid supported by an ultrathin carbon film. For the  
441 particle size distribution, we counted 126 particles with ten high-resolution STEM images.

442 TPO experiment was performed using BELCAT II (MicrotracBEL) to quantify the amount of coke  
443 deposited on the spent catalysts after 20 h of CO<sub>2</sub>-ODP at 550 °C (0.1g of the catalyst with 0.9g quartz  
444 sand). The spent catalyst placed in a quartz tube reactor was treated under flowing He (30 mL/min) at  
445 150 °C for 30 min, followed by cooling to room temperature. Then, the catalyst bed temperature was  
446 increased (40–900 °C, ramping rate: 5 °C min<sup>-1</sup>) under flowing O<sub>2</sub>/He (50%, 40 mL/min). The amount  
447 of CO<sub>2</sub> in the outlet gas was quantified by an online mass spectrometer. CO<sub>2</sub>- and He-TPSR

448 experiments were performed for coked catalysts in a similar fashion using the flow of CO<sub>2</sub>/He (10%, 30  
449 mL/min) and pure He (30 mL/min). The dispersion of Pt and Co in the catalysts (percentage of exposed  
450 Pt+Co to the total amount of Pt+Co) was measured by chemisorption of CO at room temperature. Prior  
451 to chemisorption, the catalyst (40 mg) was treated by 5% H<sub>2</sub>/Ar (30 mL/min) at 550 °C for 0.5 h,  
452 followed by cooling to ca -110 °C by liquid nitrogen with an He purge (30 mL/min). Then, introduced a  
453 pulse of 10% CO/He into the reactor and quantified the CO passed through the catalyst bed using a TCD  
454 detector. This pulse measurement was repeated until no more CO was adsorbed. The dispersion was  
455 estimated assuming a 1:1 stoichiometry of CO adsorption on Pt and/or Co.

456 Laser Raman spectroscopy experiments were carried out using a JEOL NRS-5100 spectrometer at  
457 room temperature to investigate the carbonaceous deposits over the spent catalysts, with 2 cm<sup>-1</sup>  
458 resolution of the apparatus and a 532 nm excitation source.

459 X-ray absorption fine structure (XAFS) spectra of the prepared catalysts were collected at the  
460 BL01B14 beamline of SPring-8, Japan Synchrotron Radiation Research Institute (JASRI) using Si(111)  
461 (for Co K- and Pt L<sub>III</sub>-edges) and Si(311) (for In K-edge) double-crystals as monochromators. Prior to  
462 the measurement, the catalyst was pelletized (ca. 150 mg with a diameter of 10 mm) and pretreated by  
463 H<sub>2</sub>/N<sub>2</sub> (20%, 40 mL/min) at 550 °C for 0.5 h in an in-situ quartz cell, followed by cooling to room  
464 temperature with N<sub>2</sub> purge (32 mL/min). The XAFS spectra were recorded in a transmission (In K-edge)  
465 and a fluorescence (Pt L<sub>III</sub>-, and Co K-edge: using a 19-element Ge solid-state detector) modes at room  
466 temperature. Athena and Artemis softwares ver. 0.9.25 implemented in the Demeter package were used  
467 for the analysis of the obtained XAFS spectra. FEFF8 was used for the calculation of the back-scattering  
468 amplitude and phase shift functions.<sup>42</sup> We defined the R-factor (R<sup>2</sup>) for curve-fitting as follows:  $R^2 =$   
469  $\sum_i \{k^3 \chi_i^{exp}(k) - k^3 \chi_i^{fit}(k)\}^2 / \sum_i \{k^3 \chi_i^{exp}(k)\}^2$ .

470 XPS X-ray photoelectron spectroscopy (XPS) analysis for the catalysts was carried out using a  
471 JEOL JPS-9010MC (Mg-K $\alpha$  irradiation) spectrometer. The catalysts were reduced in a quartz tube  
472 reactor under following H<sub>2</sub> (0.1 MPa, 20 mL min<sup>-1</sup>) at 550°C for 30 min, then transferred into the  
473 spectrometer using a sealed vessel and an Ar globe box without exposing to air. Binding energies were  
474 calibrated with the O 1s emission of CeO<sub>2</sub> as 529.9 eV.

475

476 **Catalytic test**

477 CO<sub>2</sub>-ODP was performed in a quartz fixed-bed reactor with 6 mm of internal diameter under an  
 478 atmospheric pressure. The catalyst (0.10 g) diluted with sea sand (0.90 g, Miyazaki Chemical, 99.9%)  
 479 was treated under flowing hydrogen (10 mL/min) at 550°C for 0.5 h prior to the catalytic reactions.  
 480 Then, the catalysts were evaluated by feeding reactant gas mixture (C<sub>3</sub>H<sub>8</sub>: CO<sub>2</sub>: He = 1:1:2, a total flow  
 481 rate of 20 mL/min). The gas phase was analyzed and quantified using an online thermal conductivity  
 482 detection gas chromatograph (Shimadzu GC-8A, column: Gaskuropack 54) equipped downstream. For  
 483 all the catalysts, C<sub>3</sub>H<sub>6</sub>, C<sub>2</sub>H<sub>4</sub>, C<sub>2</sub>H<sub>6</sub>, CH<sub>4</sub>, CO, CO<sub>2</sub>, H<sub>2</sub>O, and H<sub>2</sub> were detected as reaction products in  
 484 outlet gas. The C<sub>3</sub>H<sub>8</sub> and CO<sub>2</sub> conversions were defined as follows:  
 485

$$486 \quad \text{C}_3\text{H}_8 \text{ conversion: } X_{\text{C}_3\text{H}_8} (\%) = \frac{F_{\text{C}_3\text{H}_8}^{\text{in}} - F_{\text{C}_3\text{H}_8}^{\text{out}}}{F_{\text{C}_3\text{H}_8}^{\text{in}}} \times 100 \quad (1)$$

$$487 \quad \text{CO}_2 \text{ conversion: } X_{\text{CO}_2} (\%) = \frac{F_{\text{CO}_2}^{\text{in}} - F_{\text{CO}_2}^{\text{out}}}{F_{\text{CO}_2}^{\text{in}}} \times 100 \quad (2)$$

488

489 where,  $F_x^{\text{in}}$  and  $F_x^{\text{out}}$  indicate the inlet and outlet flow rates of  $x$  (mL · min<sup>-1</sup>), respectively.

490 In this reaction, CO can be formed from C<sub>*x*</sub>H<sub>*y*</sub> by dry reforming as well as from CO<sub>2</sub> via reverse water  
 491 gas shift reaction, which were distinguished as follows:  
 492

$$493 \quad \text{CO formed from CO}_2: F_{\text{CO}}^{\text{CO}_2} = F_{\text{CO}_2}^{\text{in}} - F_{\text{CO}_2}^{\text{out}} \quad (\text{mL} \cdot \text{min}^{-1}) \quad (3)$$

$$494 \quad \text{CO formed from C}_x\text{H}_y: F_{\text{CO}}^{\text{C}_x\text{H}_y} = F_{\text{CO}}^{\text{out}} - F_{\text{CO}}^{\text{CO}_2} \quad (\text{mL} \cdot \text{min}^{-1}) \quad (4)$$

495

496 Then, two different expressions of C<sub>3</sub>H<sub>6</sub> selectivity and yield were defined to compare with those  
 497 reported in literature.  
 498

$$499 \quad \text{C}_3\text{H}_6 \text{ sel. in C}_x\text{H}_y: S_{\text{C}_3\text{H}_6}^{\text{C}_x\text{H}_y} (\%) = \frac{F_{\text{C}_3\text{H}_6}^{\text{out}}}{F_{\text{C}_3\text{H}_6}^{\text{out}} + \frac{2}{3}F_{\text{C}_2\text{H}_6}^{\text{out}} + \frac{2}{3}F_{\text{C}_2\text{H}_4}^{\text{out}} + \frac{1}{3}F_{\text{CH}_4}^{\text{out}}} \times 100 \quad (5)$$

$$500 \quad \text{net C}_3\text{H}_6 \text{ sel.: } S_{\text{C}_3\text{H}_6} (\%) = \frac{F_{\text{C}_3\text{H}_6}^{\text{out}}}{F_{\text{C}_3\text{H}_6}^{\text{out}} + \frac{2}{3}F_{\text{C}_2\text{H}_6}^{\text{out}} + \frac{2}{3}F_{\text{C}_2\text{H}_4}^{\text{out}} + \frac{1}{3}F_{\text{CH}_4}^{\text{out}} + \frac{1}{3}F_{\text{CO}}^{\text{C}_x\text{H}_y}} \times 100 \quad (6)$$

$$501 \quad \text{C}_3\text{H}_6 \text{ yield in C}_x\text{H}_y: Y_{\text{C}_3\text{H}_6}^{\text{C}_x\text{H}_y} (\%) = \frac{X_{\text{C}_3\text{H}_8} \cdot S_{\text{C}_3\text{H}_6}^{\text{C}_x\text{H}_y}}{100} \quad (7)$$

$$502 \quad \text{net C}_3\text{H}_6 \text{ yield: } Y_{\text{C}_3\text{H}_6} (\%) = \frac{X_{\text{C}_3\text{H}_8} \cdot S_{\text{C}_3\text{H}_6}}{100} \quad (8)$$

503

504 H<sub>2</sub> yield was defined as follows:

$$505 \quad \text{H}_2 \text{ yield: } Y_{\text{H}_2} (\%) = \frac{F_{\text{H}_2}^{\text{out}}}{F_{\text{C}_3\text{H}_8}^{\text{in}}} \times 100 \quad (9)$$

506 Material balance was considered using the following scales:

507

$$508 \quad \text{carbon blance in } C_xH_y = \frac{F_{\text{C}_3\text{H}_8}^{\text{out}} + F_{\text{C}_3\text{H}_6}^{\text{out}} + \frac{2}{3}F_{\text{C}_2\text{H}_6}^{\text{out}} + \frac{2}{3}F_{\text{C}_2\text{H}_4}^{\text{out}} + \frac{1}{3}F_{\text{CH}_4}^{\text{out}}}{F_{\text{C}_3\text{H}_8}^{\text{in}}} \times 100 \quad (10)$$

$$509 \quad \text{carbon blance in } CO_x = \frac{F_{\text{CO}_2}^{\text{out}} + F_{\text{CO}}^{\text{out}}}{F_{\text{CO}_2}^{\text{in}}} \times 100 \quad (11)$$

510 total carbon blance =

$$511 \quad \frac{F_{\text{C}_3\text{H}_8}^{\text{out}} + F_{\text{C}_3\text{H}_6}^{\text{out}} + \frac{2}{3}F_{\text{C}_2\text{H}_6}^{\text{out}} + \frac{2}{3}F_{\text{C}_2\text{H}_4}^{\text{out}} + \frac{1}{3}F_{\text{CH}_4}^{\text{out}} + F_{\text{CO}_2}^{\text{out}} + \frac{1}{3}F_{\text{CO}}^{\text{out}} + F_{\text{CO}}^{\text{CO}_2}}{F_{\text{C}_3\text{H}_8}^{\text{in}} + F_{\text{CO}_2}^{\text{in}}} \times 100 \quad (12)$$

$$512 \quad \text{oxygen blance} = \frac{2F_{\text{CO}_2}^{\text{out}} + F_{\text{CO}}^{\text{out}} + F_{\text{H}_2\text{O}}^{\text{out}}}{2F_{\text{CO}_2}^{\text{in}}} \times 100 \quad (13)$$

513

514 Deactivation constant, mean catalyst life, CO<sub>2</sub> utilization efficiency, turnover frequency (TOF), average  
515 coke selectivity, and turnover number of coke were defined as follows.

516

$$517 \quad \text{Deactivation constant: } k_d = \left\{ \ln \left( \frac{1 - X_{\text{C}_3\text{H}_8}^f}{X_{\text{C}_3\text{H}_8}^f} \right) - \ln \left( \frac{1 - X_{\text{C}_3\text{H}_8}^i}{X_{\text{C}_3\text{H}_8}^i} \right) \right\} (t^f - t^i)^{-1} \quad (14)$$

$$518 \quad \text{Mean catalyst life: } \tau = \frac{1}{k_d} \quad (15)$$

$$519 \quad \text{CO}_2 \text{ utilization efficiency (\%)} = X_{\text{CO}_2} \left( 1 - \frac{|X_{\text{CO}_2} - Y_{\text{C}_3\text{H}_6}|}{X_{\text{CO}_2} + Y_{\text{C}_3\text{H}_6}} \right) \quad (16)$$

$$520 \quad \text{TOF}_{\text{C}_3\text{H}_8/\text{CO}_2} (\text{site}^{-1}\text{min}^{-1}) = \frac{M_{\text{C}_3\text{H}_8/\text{CO}_2}^{\text{in}} \times X_{\text{C}_3\text{H}_8/\text{CO}_2}^i}{n_{\text{Pt+Co}} \times D} \quad (17)$$

$$521 \quad \text{average coke selectivity: } S_c (\%) = \frac{\frac{1}{3}n_c^t}{\int_0^t (F_{\text{C}_3\text{H}_8}^{\text{in}} - F_{\text{C}_3\text{H}_8}^{\text{out}}) dt} \times 100 \quad (18)$$

$$522 \quad \text{TON}_{\text{coke}} (\text{site}^{-1}) = \frac{n_c^t}{n_{\text{Pt+Co}} \times D} \quad (19)$$

523

524 where,  $X_{C_3H_8}^i$  and  $X_{C_3H_8}^f$  indicate the initial ( $t^i$ : 0.5 h) and final ( $t^f$ : 20 h)  $X_{C_3H_8}$ , respectively.  
525  $M_{C_3H_8/CO_2}^{in}$  and  $M_{C_3H_8/CO_2}^{out}$  are the inlet and outlet molar flow rates (mol/min) of  $C_3H_8$  or  $CO_2$ ,  
526 respectively.  $n_{Pt+Co}$  and  $D$  correspond to the mole of active metal in the catalyst and its dispersion  
527 estimated by CO chemisorption, respectively.  $n_C^t$  indicates mole of coke accumulated at time on stream  
528 of  $t$  ( $x = C$ ). The second term in the parenthesis of eq (16) represents the degree of deviation between  
529  $X_{CO_2}$  and  $Y_{C_3H_6}$ . We also used a flame ionization detection gas chromatograph (FID-GC: Shimadzu  
530 GC-14B, column: Porapak-Q) equipped with a methanizer (Shimadzu MTN-1) to detect oxygenated  
531 products. All the catalytic tests for kinetic analysis were performed under differential conditions by  
532 adjusting the catalyst amount, where the reactant conversion was lower than 15% (typically 5~10%).  
533

### 534 **Computational details**

535 Periodic DFT calculations were performed using the CASTEP code<sup>43</sup> with Vanderbilt-type ultrasoft  
536 pseudopotentials and the revised version of Perdew–Burke–Ernzerhof exchange–correlation functional  
537 based on the generalized gradient approximation.<sup>44</sup> The plane-wave basis set was truncated at a kinetic  
538 energy of 360 eV. A Fermi smearing of 0.1 eV was utilized. Dispersion correlations were considered  
539 using the Tkatchenko–Scheffler method with a scaling coefficient of  $s_R = 0.94$  and a damping parameter  
540 of  $d = 20$ .<sup>45</sup> The reciprocal space was sampled using a  $k$ -point mesh with a spacing of typically  $0.04 \text{ \AA}^{-1}$ ,  
541 as generated by the Monkhorst–Pack scheme.<sup>46</sup> Geometry optimizations and transition state (TS)  
542 searches were performed on supercell structures using periodic boundary conditions. The surfaces were  
543 modeled using metallic slabs with a thickness of four atomic layers with  $13 \text{ \AA}$  of vacuum spacing. We  
544 chose  $Pt_2In_3(012)$  as the most stable surface, which has the highest surface atom density and diffraction  
545 intensity.<sup>47,48</sup>  $Pt_2In_3(012)$ –Co was constructed as a model of the surface  $(Pt_{1-x}Co_x)_2In_3$  pseudo binary  
546 alloy by replacing one of the surface Pt atoms of  $Pt_2In_3(012)$ . The unit cells were  $(2 \times 2)$  for Pt(111),  $(1$   
547  $\times 1)$  for  $C_3H_8$  dehydrogenation on  $Pt_2In_3(012)$ (–Co), and  $(1 \times 2)$  for  $CO_2$  reduction on  $Pt_2In_3(012)$ (–Co).  
548 Geometry optimizations were performed using the Broyden–Fletcher–Goldfarb–Shanno (BFGS)  
549 algorithm.<sup>49</sup> The unit cell size of the bulk material (Pt and  $Pt_2In_3$ ) was firstly optimized, followed by  
550 modeling the slab structure and surface relaxation with the size of the supercell fixed. The convergence  
551 criteria for structure optimization and energy calculation were set to (a) an SCF tolerance of  
552  $1.0 \times 10^{-6}$  eV per atom, (b) an energy tolerance of  $1.0 \times 10^{-5}$  eV per atom, (c) a maximum force

553 tolerance of  $0.05 \text{ eV \AA}^{-1}$ , and (d) a maximum displacement tolerance of  $1.0 \times 10^{-3} \text{ \AA}$ .

554 The adsorption energy was defined as follows:  $E_{\text{ad}} = E_{\text{A-S}} - (E_{\text{S}} + E_{\text{A}})$ , where  $E_{\text{A-S}}$  is the energy of  
555 the slab together with the adsorbate,  $E_{\text{A}}$  is the total energy of the free adsorbate, and  $E_{\text{S}}$  is the total  
556 energy of the bare slab. The adsorption energy for an oxygen-preadsorbed slab was calculated using  $E_{\text{SH}}$ ,  
557 which is the total energy of the oxygen-adsorbed slab, instead of using  $E_{\text{S}}$ . The d band center ( $\varepsilon_{\text{d}}$ ) was  
558 defined as the average energy of the occupied d band relative to the Fermi level as follows:

559

$$560 \quad \varepsilon_{\text{d}} = \frac{\int_{-\infty}^0 E \rho_{\text{d}}(E) \text{ d}E}{\int_{-\infty}^0 \rho_{\text{d}}(E) \text{ d}E} \quad (20)$$

561

562 where  $\rho_{\text{d}}$  is the density of states projected to d orbitals.

563 The transition state (TS) search was performed using the complete linear synchronous  
564 transit/quadratic synchronous transit (LST/QST) method.<sup>50,51</sup> Linear synchronous transit maximization  
565 was performed, followed by energy minimization in the directions conjugating to the reaction pathway.  
566 The approximated TS was used to perform QST maximization with conjugate gradient minimization  
567 refinements. This cycle was repeated until a stationary point was found. Convergence criterion for the  
568 TS calculations were set to root-mean-square forces on an atom tolerance of  $0.05 \text{ eV \AA}^{-1}$ .

569 The activation energy ( $E_{\text{A}}$ ) was determined as the largest energy barrier among all the focused steps:  
570 for  $\text{CO}_2$  conversion;  $\text{CO}_2$  activation, for  $\text{C}_3\text{H}_8$  conversion, the 1st or 2nd C–H activation. We also  
571 consider theoretical apparent activation energy,  $E_{\text{A}}^*$ , for the comparison with the experimental values.  
572 This is identical to  $E_{\text{A}}$  except when the initial state for  $E_{\text{A}}$  is a weakly adsorbed state, like physisorption,  
573 where the apparent activation energy should be expressed as  $E_{\text{A}}^* = E_{\text{A}} + E_{\text{ad}}$  as often considered in  
574 literature.<sup>43</sup> In this study, the 1st C–H activation on  $\text{Pt}_2\text{In}_3$  falls into this case:  $E_{\text{A}}^* = E_{\text{A}} (153.3) + E_{\text{ad}}$   
575  $(-13.2) = 140.1 \text{ kJ/mol}$ .

576

577 Vibrational frequencies of the adsorbates were computed by phonon calculation based on harmonic  
578 approximation using the finite displacement method in CASTEP. Fractional positions of all the metal  
579 atoms were fixed so that only C, H, and O atoms were considered for phonon calculation. The  
580 contribution of solid surface to the vibrational terms, which is typically much lower than that of  
581 adsorbates, was ignored. The threshold for energy convergence for each iteration was set to  $10^{-10} \text{ eV per}$   
582 atom. The entropy ( $S$ ), Gibbs free energy ( $G$ ), and partition function ( $q$ ) of each species were estimated

583 at 550 °C using the calculated vibrational frequencies ( $\nu_n$ ) as follows:<sup>52</sup>

584

$$585 \quad G(T, P) = E_e + E_{trans} + E_{rot} + E_{vib} + PV - T(S_{trans} + S_{rot} + S_{vib}) \quad (21)$$

586 where,  $E_e$  is the electronic energy,

$$587 \quad E_{trans} = \frac{3}{2}RT \quad (22), \quad E_{rot} = RT \quad (23) \quad (\text{for linear molecule}),$$

$$588 \quad E_{rot} = \frac{3}{2}RT \quad (24) \quad (\text{for nonlinear molecule}), \quad E_{vib} = R \sum_n \frac{h\nu_n}{k_B} \left( \frac{1}{2} + \frac{1}{e^{h\nu_n/k_B T} - 1} \right) \quad (25)$$

$$589 \quad S_{trans} = R \left( \ln q_{trans} + \frac{5}{2} \right) \quad (26), \quad \text{where} \quad q_{trans} = \left( \frac{2\pi m k_B T}{h^2} \right)^{3/2} \frac{k_B T}{P} \quad (27)$$

$$590 \quad S_{rot} = R(\ln q_{rot} + 1) \quad (28) \quad (\text{for linear molecule}), \quad \text{where} \quad q_{rot} = \frac{1}{\sigma} \left( \frac{8\pi^2 k_B T}{h^2} \right) \times I \quad (29)$$

$$591 \quad S_{rot} = R \left( \ln q_{rot} + \frac{3}{2} \right) \quad (30) \quad (\text{for nonlinear molecule}),$$

$$592 \quad \text{where} \quad q_{rot} = \frac{\sqrt{\pi}}{\sigma} \left( \frac{8\pi^2 k_B T}{h^2} \right)^{3/2} \times \sqrt{I_x I_y I_z} \quad (31)$$

$$593 \quad S_{vib} = R \sum_n \left( \frac{h\nu_n/k_B}{e^{h\nu_n/k_B T} - 1} - \ln(1 - e^{-h\nu_n/k_B T}) \right) \quad (32)$$

594

595 where,  $I$  is the moment of inertia,  $\sigma$  is the rotational symmetry number, and  $m$  is the mass of the  
596 molecule. For surface species, the rotational and translational contributions were converted into  
597 vibrational modes and the  $PV$  term was approximated to be negligible compared with the energetic  
598 terms; therefore, the Gibbs free energy for surface species was considered as follows:  $G(T, P) = E_e +$   
599  $E_{vib} - TS_{vib}$ . Neglecting the spurious frequencies contributes to the enthalpy and entropy; hence,  
600 spurious frequencies lower than  $100 \text{ cm}^{-1}$  were replaced with  $50 \text{ cm}^{-1}$  for all the structures to provide  
601 consistent results as reported in literature.<sup>53</sup> The properties of the reactant ( $\text{C}_3\text{H}_8$  and  $\text{CO}_2$ ) and product  
602 ( $\text{C}_3\text{H}_6$ ,  $\text{CO}$ , and  $\text{H}_2\text{O}$ ) molecules in gas phase were calculated using an ideal gas approximation at  
603  $550 \text{ °C}$  and their translational and rotational contributions were evaluated at relative pressures ( $P/P^0$ ) of  
604 0.24 and 0.01, respectively.

605

## 606 **Data Availability**

607 All data is available from the authors upon reasonable request, because the authors need to confirm the  
608 purpose.

610 **References**

- 611 1. Amghizar, I., Vandewalle, L. A., Van Geem, K. M. & Marin, G. B. New Trends in Olefin Production. *Engineering* **3**,  
612 171–178 (2017).
- 613 2. Sattler, J. J. H. B., Ruiz-Martinez, J., Santillan-Jimenez, E. & Weckhuysen, B. M. Catalytic Dehydrogenation of  
614 Light Alkanes on Metals and Metal Oxides. *Chem. Rev.* **114**, 10613–10653 (2014).
- 615 3. Bhasin, M. M., McCain, J. H., Vora, B. V., Imai, T. & Pujadó, P. R. Dehydrogenation and oxydehydrogenation of  
616 paraffins to olefins. *Appl. Catal. A Gen.* **221**, 397–419 (2001).
- 617 4. Wang, S. & Zhu, Z. H. Catalytic conversion of alkanes to olefins by carbon dioxide oxidative dehydrogenation - A  
618 review. *Energy and Fuels* **18**, 1126–1139 (2004).
- 619 5. Atanga, M. A., Rezaei, F., Jawad, A., Fitch, M. & Rownaghi, A. A. Oxidative dehydrogenation of propane to  
620 propylene with carbon dioxide. *Appl. Catal. B Environ.* **220**, 429–445 (2018).
- 621 6. Ansari, M. B. & Park, S. E. Carbon dioxide utilization as a soft oxidant and promoter in catalysis. *Energy Environ.*  
622 *Sci.* **5**, 9419–9437 (2012).
- 623 7. Gomez, E. *et al.* Combining CO<sub>2</sub> reduction with propane oxidative dehydrogenation over bimetallic catalysts. *Nat.*  
624 *Commun.* **9**, 1–6 (2018).
- 625 8. Ruthwik, N., Kavya, D., Shadab, A., Lingaiah, N. & Sumana, C. Thermodynamic analysis of chemical looping  
626 combustion integrated oxidative dehydrogenation of propane to propylene with CO<sub>2</sub>. *Chem. Eng. Process. Process*  
627 *Intensif.* **153**, 107959 (2020).
- 628 9. Farnaz, T. Z., Abbas T., Khodayer, G. & Saeed, S. Thermodynamic Equilibrium Analysis of Propane  
629 Dehydrogenation with Carbon Dioxide and Side Reactions. *Chem. Eng. Commun.* **203**, 557–565 (2016).
- 630 10. Osaki, T. & Mori, T. Kinetics of the reverse-Boudouard reaction over supported nickel catalysts. *React. Kinet. Catal.*  
631 *Lett.* **89**, 333–339 (2006).
- 632 11. Jacobson, M. Z. Review of solutions to global warming, air pollution, and energy security. *Energy Environ. Sci.* **2**,  
633 148–173 (2009).
- 634 12. Tollefson, J. World's carbon emissions set to spike by 2% in 2017. *Nature* **551**, 283–283 (2017).
- 635 13. Shishido, T., Shimamura, K., Teramura, K. & Tanaka, T. Role of CO<sub>2</sub> in dehydrogenation of propane over Cr-based  
636 catalysts. *Catal. Today* **185**, 151–156 (2012).
- 637 14. Botavina, M. A. *et al.* Towards efficient catalysts for the oxidative dehydrogenation of propane in the presence of  
638 CO<sub>2</sub>: Cr/SiO<sub>2</sub> systems prepared by direct hydrothermal synthesis. *Catal. Sci. Technol.* **6**, 840–850 (2016).
- 639 15. Xu, B., Zheng, B., Hua, W., Yue, Y. & Gao, Z. Support effect in dehydrogenation of propane in the presence of CO<sub>2</sub>  
640 over supported gallium oxide catalysts. *J. Catal.* **239**, 470–477 (2006).
- 641 16. Chen, M. *et al.* Study in support effect of In<sub>2</sub>O<sub>3</sub>/MO<sub>x</sub> (M = Al, Si, Zr) catalysts for dehydrogenation of propane in the  
642 presence of CO<sub>2</sub>. *Appl. Catal. A Gen.* **407**, 20–28 (2011).
- 643 17. Nowicka, E. *et al.* Elucidating the Role of CO<sub>2</sub> in the Soft Oxidative Dehydrogenation of Propane over Ceria-Based  
644 Catalysts. *ACS Catal.* **8**, 3454–3468 (2018).
- 645 18. Baek, J., Yun, H. J., Yun, D., Choi, Y. & Yi, J. Preparation of highly dispersed chromium oxide catalysts supported on  
646 mesoporous silica for the oxidative dehydrogenation of propane using CO<sub>2</sub>: Insight into the nature of catalytically  
647 active chromium sites. *ACS Catal.* **2**, 1893–1903 (2012).

- 648 19. Wang, H. M., Chen, Y., Yan, X., Lang, W. Z. & Guo, Y. J. Cr doped mesoporous silica spheres for propane  
649 dehydrogenation in the presence of CO<sub>2</sub>: Effect of Cr adding time in sol-gel process. *Microporous Mesoporous Mater.*  
650 **284**, 69–77 (2019).
- 651 20. Jeon, J., Kon, K. , Toyao, T., Shimizu, K. & Furukawa, S. Design of Pd-based pseudo-binary alloy catalysts for  
652 highly active and selective NO reduction. *Chem. Sci.* **10**, 4148–4162 (2019).
- 653 21. Nakaya, Y., Miyazaki, M., Yamazoe, S., Shimizu, K. & Furukawa, S. Active, Selective, and Durable Catalyst for  
654 Alkane Dehydrogenation Based on a Well-Designed Trimetallic Alloy. *ACS Catal.* **10**, 5163–5172 (2020).
- 655 22. Nakaya, Y., Hirayama, J., Yamazoe, S., Shimizu, K. & Furukawa, S. Single-atom Pt in intermetallics as an ultrastable  
656 and selective catalyst for propane dehydrogenation. *Nat. Commun.* **11**, 3–9 (2020).
- 657 23. Sun, G. *et al.* Breaking the scaling relationship via thermally stable Pt/Cu single atom alloys for catalytic  
658 dehydrogenation. *Nat. Commun.* **9**, (2018).
- 659 24. Ryoo, R. *et al.* Rare-earth–platinum alloy nanoparticles in mesoporous zeolite for catalysis. *Nature* **585**, 221–224  
660 (2020).
- 661 25. Liu, B. & Greeley, J. Decomposition pathways of glycerol via C-H, O-H, and C-C bond scission on Pt(111): A  
662 density functional theory study. *J. Phys. Chem. C* **115**, 19702–19709 (2011).
- 663 26. Álvarez, A. *et al.* CO<sub>2</sub> Activation over Catalytic Surfaces. *ChemPhysChem* **18**, 3135–3141 (2017).
- 664 27. Studt, F. *et al.* Discovery of a Ni-Ga catalyst for carbon dioxide reduction to methanol. *Nat. Chem.* **6**, 320–324  
665 (2014).
- 666 28. Furukawa, S. & Komatsu, T. Intermetallic Compounds: Promising Inorganic Materials for Well-Structured and  
667 Electronically Modified Reaction Environments for Efficient Catalysis. *ACS Catal.* **7**, 735–765 (2017).
- 668 29. Pakhare, D. & Spivey, J. A review of dry (CO<sub>2</sub>) reforming of methane over noble metal catalysts. *Chem. Soc. Rev.* **43**,  
669 7813–7837 (2014).
- 670 30. Kopač, D., Likozar, B. & Huš, M. How Size Matters: Electronic, Cooperative, and Geometric Effect in  
671 Perovskite-Supported Copper Catalysts for CO<sub>2</sub> Reduction. *ACS Catal.* **10**, 4092–4102 (2020).
- 672 31. Zhang, W. *et al.* Size Dependence of Pt Catalysts for Propane Dehydrogenation: From Atomically Dispersed to  
673 Nanoparticles. *ACS Catal.* **10**, 12932–12942 (2020).
- 674 32. Zhu, J. *et al.* Size-Dependent Reaction Mechanism and Kinetics for Propane Dehydrogenation over Pt Catalysts.  
675 *ACS Catal.* **5**, 6310–6319 (2015).
- 676 33. You, A., Be, M. A. Y. & In, I. Phase equilibria in the Pt-In-P system. **4398**, (1998).
- 677 34. Barbosa, R. L. *et al.* Methanol steam reforming over indium-promoted Pt/Al<sub>2</sub>O<sub>3</sub> catalyst: Nature of the active surface.  
678 *J. Phys. Chem. C.* **117**, 6143–6150 (2013).
- 679 35. Thu D. Nguyen, F. E. C. and G. T. CO<sub>2</sub> Assisted Ethane Oxidative Dehydrogenation Over MoO<sub>3</sub> and V<sub>2</sub>O<sub>5</sub> catalysts  
680 supported on Reducible CeO<sub>2</sub>-TiO<sub>2</sub>. 43–57 (1993).
- 681 36. Melaet, G. *et al.* Evidence of highly active cobalt oxide catalyst for the Fischer-Tropsch synthesis and CO<sub>2</sub>  
682 hydrogenation. *J. Am. Chem. Soc.* **136**, 2260–2263 (2014).
- 683 37. Wang, L., Liu, H., Chen, Y. & Yang, S. Reverse water–gas shift reaction over co-precipitated Co–CeO<sub>2</sub> catalysts:  
684 Effect of Co content on selectivity and carbon formation. *Int. J. Hydrogen Energy* **42**, 3682–3689 (2017).
- 685 38. Zhang, W. *et al.* Size Dependence of Pt Catalysts for Propane Dehydrogenation: from Atomically Dispersed to  
686 Nanoparticles. *ACS Catal.* **10**, 12932–12942 (2020).
- 687 39. Wang, Y., Furukawa, S. & Yan, N. Identification of an Active NiCu Catalyst for Nitrile Synthesis from Alcohol. *ACS*

- 688 *Catal.* **9**, 6681–6691 (2019).
- 689 40. Hammer, B. & Norskov, J. K. Why gold is the noblest of all the metals. *Nature* **376**, 238–240 (1995).
- 690 41. LiBretto, N. J., Yang, C., Ren, Y., Zhang, G. & Miller, J. T. Identification of Surface Structures in Pt<sub>3</sub>Cr Intermetallic  
691 Nanocatalysts. *Chem. Mater.* **31**, 1597–1609 (2019).
- 692 42. Ankudinov, A. & Ravel, B. Real-space multiple-scattering calculation and interpretation of x-ray-absorption  
693 near-edge structure. *Phys. Rev. B - Condens. Matter Mater. Phys.* **58**, 7565–7576 (1998).
- 694 43. Segall, M. D. *et al.* First-principles simulation: Ideas, illustrations and the CASTEP code. *J. Phys. Condens. Matter*  
695 **14**, 2717–2744 (2002).
- 696 44. Hammer, B., Hansen, L. B. & Nørskov, J. K. Improved adsorption energetics within density-functional theory using  
697 revised Perdew-Burke-Ernzerhof functionals. *Phys. Rev. B - Condens. Matter Mater. Phys.* **59**, 7413–7421 (1999).
- 698 45. Tkatchenko, A. & Scheffler, M. Accurate molecular van der Waals interactions from ground-state electron density  
699 and free-atom reference data. *Phys. Rev. Lett.* **102**, 6–9 (2009).
- 700 46. Hu, K. *et al.* Boosting electrochemical water splitting: via ternary NiMoCo hybrid nanowire arrays. *J. Mater. Chem.*  
701 *A* **7**, 2156–2164 (2019).
- 702 47. Jana, R. & Peter, S. C. One-pot solvothermal synthesis of ordered intermetallic Pt<sub>2</sub>In<sub>3</sub> as stable and efficient  
703 electrocatalyst towards direct alcohol fuel cell application. *J. Solid State Chem.* **242**, 133–139 (2016).
- 704 48. Ye, J., Liu, C. & Ge, Q. A DFT study of methanol dehydrogenation on the PdIn(110) surface. *Phys. Chem. Chem.*  
705 *Phys.* **14**, 16660–16667 (2012).
- 706 49. Fischer, T. H. & Almlöf, J. General methods for geometry and wave function optimization. *J. Phys. Chem.* **96**, 9768–  
707 9774 (1992).
- 708 50. Govind, N., Petersen, M., Fitzgerald, G., King-Smith, D. & Andzelm, J. A generalized synchronous transit method  
709 for transition state location. *Comput. Mater. Sci.* **28**, 250–258 (2003).
- 710 51. Halgren, T. A. & Lipscomb, W. N. The synchronous-transit method for determining reaction pathways and locating  
711 molecular transition states. *Chem. Phys. Lett.* **49**, 225–232 (1977).
- 712 52. Wang, J. *et al.* A highly selective and stable ZnO-ZrO<sub>2</sub> solid solution catalyst for CO<sub>2</sub> hydrogenation to methanol. *Sci.*  
713 *Adv.* **3**, 1–11 (2017).
- 714 53. Schoonheydt, R. A. & Weckhuysen, B. M. Physisorption and chemisorption of alkanes and alkenes in H-FAU: a  
715 combined ab initio–statistical thermodynamics study. *Phys. Chem. Chem. Phys.* **11**, 2794–2798 (2009).
- 716

## 717 **Acknowledgement**

718 This work was supported by JSPS KAKENHI (Grant Numbers 17H01341, 17H04965, and 20H02517),  
719 MEXT project Element Strategy Initiative (JPMXP0112101003), JST CREST (JPMJCR17J3), JST  
720 PRESTO (JPMJPR19T7), and the Collaborative Research Projects of Laboratory for Materials and  
721 Structures, Institute of Innovative Research, Tokyo Institute of Technology. The XAFS analysis was  
722 performed with the approval of JASRI (No. 2019B1620 and 2019B1469). We appreciate the technical  
723 staffs of Research Institute for Electronic Science, Dr. Yuta Nakasaka, and Mr. Kah Wei Ting,  
724 Hokkaido University for help with HAADF-STEM, Raman, and XPS analyses, respectively.

725 Computation time was provided by the supercomputer systems in Institute for Chemical Research,  
726 Kyoto University.

727

728 **Author contributions**

729 S.F. and F.X. design the research and co-wrote the manuscript in discussion. F.X. performed all the  
730 experimental works. Y.N. contributed to XAFS and XPS studies. S.F. conducted all the computational  
731 and kinetic studies. S.Y. contributed to free energy calculation. S.F., F.X., Y.N., S.Y., and K.S.  
732 discussed the data and commented on the manuscript.

733

734 **Competing interests**

735 The authors declare no competing interests.